Developing a Nanoplatform to Prevent the Spread of Parkinson's Disease

By India Jade Boyton, BSc

COMMERCIAL-IN-CONFIDENCE

A thesis submitted in partial fulfilment of the requirements for the degree

Master of Research (MRes)

MACQUARIE University
SYDNEY·AUSTRALIA

Department of Molecular Sciences (MolSci)

Macquarie University

18th of November 2019

Acknowledgements

Firstly, I would like to express my thanks to my supervisor's Dr Andrew Care and Dr Lyndsey Collins-Praino for their amazing support, guidance, and patience over this year. Their enthusiasm in this project has been inspiring and has fostered my interest to continue working in the field.

I would also like to thank the rest of the students in our research group for making the lab and office such a welcoming environment. In particular, I would like to thank Alex, Dominik, Dennis, and Sandra for answering my many questions and teaching me all my lab skills.

I would like to express gratitude to Dr Mark Hutchinson and the ARC Centre of Excellence for Nanoscale BioPhotonics (CNBP) for providing financial support and a nurturing environment to present my work and connect with other researchers. I'd like to particularly thank Professor Nicolle Packer, Dr Liisa Kautto, and Dr Edward Moh from the MQ CNBP node for providing valuable advice and teaching me lab techniques. I would also like to thank Dr Sophie Goodchild for her incredible support and training in spectroscopy techniques and inspiring my newfound interest in the area.

A big thank you goes to my family and friends, whose support and love has helped me get through this year.

Finally, I would like to give my heartfelt thanks to Charles. Your continuous support, understanding, love, (and IT assistance) has meant everything.

Declaration

This thesis titled **"Developing a Nanoplatform to Prevent the Spread of Parkinson's Disease"** is representative of the research study conducted between January 2019 and November 2019 for the completion of Master of Research degree in Molecular Sciences at Macquarie University, New South Wales, Australia. Where appropriate, work done in collaboration with other groups or individuals and the material provided by them has been acknowledged, and otherwise to the best of my knowledge is my own work and original.

This thesis is formatted according to Master of Research guidelines prescribed by the Faculty of Science & Engineering and Molecular Sciences and no part of this thesis has been submitted for qualification or assessment to any other institution.

The following biosafety approval was obtained for the work carried out in this thesis:

- Exempt dealing:
  "Production of a protein nanocage, its variants, and its protein cargoes" (Ref. No. 0521)

India Boyton

Student ID: 43240070

Presentations

Oral presentation:

I. Boyton, S. Goodchild, D. Diaz, F. Sandra & A. Care (2019) 'Elucidating the cargo-loading biomechanics of self-assembling encapsulin nanocages'. *6th Annual Centre for Nanoscale BioPhotonics Conference, Adelaide, Australia.*

3-Minute-Thesis oral and poster presentation:

I. Boyton, S. Goodchild, D. Diaz, F. Sandra & A. Care (2019) 'Characterising the unique cargo-loading their unique self-assembling and cargo-loading capabilities'. *11th International Nanomedicine Conference, Sydney, Australia.*

Poster presentation:

I. Boyton, S. Goodchild, D. Diaz, F. Sandra & A. Care (2019) 'Encapsulin nanocages: understanding the mechanisms behind their unique self-assembling and cargo-loading capabilities'. *2nd Annual BioNetwork Research Symposium, Sydney, Australia.*

Abstract

Parkinson's disease (PD) spreads in the brain via the release of the protein α-synuclein from diseased neurons into the extracellular space, where nearby healthy brain cells take it up, triggering misfolding and aggregation of α-synuclein in those cells. Thus, pathology spreads in the brain, leading to the symptoms of PD. The overarching aim of this project was to investigate the potential of a novel protein nanocage system for the targeted capture of abnormal α-synuclein, preventing its transmission between brain cells and halting PD progression. Encapsulin protein nanocages selectively self-assemble around proteins tagged with a unique encapsulation signal peptide (ESig), encapsulating them. To better understand this process, the biophysical mechanisms and physicochemical factors underlying encapsulin disassembly/reassembly was characterised using spectroscopic techniques. Encapsulin was found to reversibly disassemble in extreme guanidine hydrochloride (4-7 M) and alkaline conditions and then reassemble within 6-8 hours when returned to normal conditions. Encapsulin disassembly/reassembly conditions were optimised and applied to successfully capture untagged superfolder green fluorescent protein. These results will help pave the way towards the capture of untagged pathological α-synuclein, and the potential future development of a capture system that halts the progression of PD in *in vitro* models.

List of Abbreviations

AA	Amino acid
AuNF	Nanoflower-like gold nanoparticle
BBB	Blood-brain barrier
CCMV	Cowpea chlorotic mottle virus
CD	Circular dichroism
CNL	Chitosan nanoparticles containing L-DOPA
CNS	Central nervous system
CUR-AAS-MSNPs	Curcumin-loaded amine-functionalised mesoporous silica nanoparticles
CV	Column volumes
DA	Dopamine agonist
DLB	Dementia with Lewy bodies
DLS	Dynamic light scattering
DTT	Dithiothreitol
ELISA	Enzyme-linked immunosorbent assay
ESig	Encapsulation signal
FDA	Food and Drug Agency
GFPnb-ESig	Anti-sfGFP nanobody tagged with 30 aa ESig
GuHCl	Guanidine hydrochloride
HEPES	4-(2-hydroxyethyl)-1-piperazineethanesulfonic acid
ITF	Intrinsic tryptophan fluorescence
IPTG	Isopropyl-β-d-thiogalactopyranoside
Lf-R-NPs	Lactoferrin functionalised Rotigotine nanoparticles
(LAT)-1	Large amino acid transporter
LC-MS/MS	Liquid chromatography-tandem mass spectrometry
LDH	Layered double hydroxide
L-DOPA	Levodopa
LV	Lentiviral vector
LB	Luria-Bertani media
MAP2	Microtubule associated protein 2
MAO-B	Monoamine oxidase type B
MX	*Myxococcus xanthus*
NGF	Nerve growth factor
NIPAm-AA	N-isopropylacrylamide and acrylic acid
NP	Nanoparticle
OD	Optical density
PAGE	Polyacrylamide gel electrophoresis
PD	Parkinson’s Disease
PEG	Poly(ethylene-glycol)

P-gp	P-glycoprotein
PEI	Polyethylenimine
PLGA	Poly(lactic-co-glycolic acid)
PS80	Polysorbate 80
QT	*Quasibacillus thermotolerans*
RT	Room temperature
SWCNT	Single walled carbon nanotubes
SDS	Sodium dodecyl sulfate
SEC	Size exclusion chromatography
sfGFP	Superfolded green fluorescent protein
shRNA	Short hairpin ribonucleic acid
siRNA	Small interfering ribonucleic acid
Syn2nb-ESig	Anti-α-synuclein nanobody tagged with 30 aa ESig
TEM	Transmission electron microscopy
TM	*Thermotoga maritima*
UAR	Uranyl acetate
UV-Vis	Ultraviolet-visible spectroscopy
VLP	Virus-like particle

Table of Contents

Chapter 1: Nanoparticles in the Treatment of Parkinson's Disease

1.1 Parkinson's Disease (PD)

Neurodegenerative disorders are characterised by a decline in physical and cognitive function caused by the progressive degeneration of neurons [1]. The second most common neurodegenerative disorder is Parkinson's Disease (PD), with a global estimate of 7–10 million cases [2]. As the likelihood of developing PD increases with age, the prevalence of this disease is expected to dramatically rise due to an aging population [2].

PD is clinically characterised by motor features such as slowness of movement, muscle rigidity, and tremors, along with non-motor features, including cognitive dysfunction and dementia [3]. Pathologically, PD is characterised by the loss of dopaminergic neurons within the substantia nigra *pars compacta*, and the subsequent decrease of dopamine levels within the striatum [4]. Dopamine is a neurotransmitter responsible for modulating multiple brain functions including cognition and voluntary movement [5]. In addition to loss of dopaminergic neurons, PD is pathologically classified by the presence of intracellular aggregates of the misfolded fibrillary protein α-synuclein, known as Lewy bodies, throughout the brain according to the Braak staging model [6]. In recent years, a growing body of evidence suggests that misfolded α-synuclein can also be exocytosed by diseased neurons into the extracellular space, where it can be taken up by healthy nearby neurons via endocytosis [7] (Fig.1). The transmission of extracellular α-synuclein into recipient neurons cause endogenous intracellular α-synuclein within these recipient neurons to misfold and aggregate, thus spreading α-synuclein pathology throughout the brain [7]. Interestingly, the staging of Lewy body pathology is known to correlate with the progression of neurodegeneration and the worsening of symptoms observed in PD [6]. The current gold standard for the treatment of PD is orally administered Levodopa (L-DOPA), which is a metabolic precursor of dopamine that is enzymatically converted into dopamine, increasing its concentration in the brain [8]. However, L-DOPA and all other approved PD treatment options only ease the symptoms, and do not modify the mechanisms that drive the disease.

In addition to only providing symptomatic relief, many approved therapeutics used for the treatment of PD show poor clinical efficacy and adverse side-effects [9]. Currently, PD therapies that target the pathological components of PD (i.e. α-synuclein and other PD-

associated proteins, neuroinflammation, and mitochondrial dysfunction) are in various stages of research [10]. However, all disease-modifying agents that have been developed thus far have failed in clinical trials [10]. Furthermore, existing drugs used in both symptomatic and disease-modifying therapies are often limited by poor solubility and bioavailability, short blood-circulation times, inadequate targeting specificity and insufficient blood-brain barrier (BBB) penetration [11].

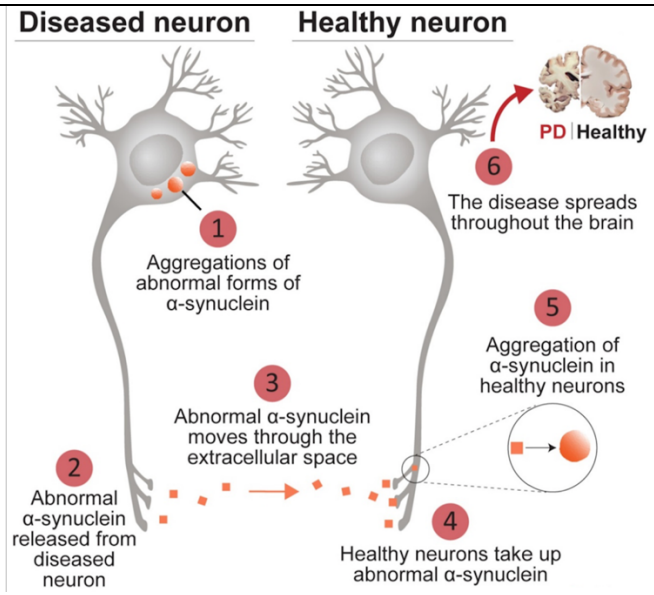

Figure 1: Model of extracellular release and transmission of α-synuclein (orange squares) from diseased to nearby healthy neurons (steps 1-6, red), resulting in the spread of PD pathology throughout the brain.

1.2 Designing Nanoparticle-based Drug Delivery Systems for the Treatment of PD

The BBB is a highly selective physiological barrier situated between the parenchyma of the brain and the lumen of central nervous system (CNS) blood vessels. It controls the permeation of molecules both physically, through tight junctions, and enzymatically, though cytosolic and membrane associated enzymes [17]. The BBB remains a major obstacle in treating brain disorders, as more than 95% of Food and Drug Agency (FDA)-approved drugs are unable to pass the BBB at a concentration that is pharmacologically sufficient [12]. As a consequence, the development of effective strategies to facilitate the transport of therapeutic agents across the BBB is vital to advancing treatments for neurodegenerative disorders.

Nanoparticles (NPs) are promising delivery vehicles for anti-PD therapeutics, with some NPs demonstrating the ability to pass through the BBB via receptor-mediated transport [13]. Herein, NPs are functionalised with ligands that enable them to bind to surface receptors

on endothelial cells of the BBB [12]. The delivery of drugs through these transport routes can then be achieved in two ways: (i) NPs are endocytosed into endothelial cells and release their cargo into the cell cytoplasm, which then undergoes exocytosis into the CNS environment; or (ii) the entire NP system penetrates through the BBB via transcytosis and directs the delivery of the cargo to the targeted site [12]. The effectiveness of this approach has been demonstrated by coating poly(lactide) NPs with the hydrophilic surfactant polysorbate 80 (PS80) [14]. PS80 mediates the adsorption of apolipoproteins present in blood onto the surface of NPs, which then allows NPs to bind to low-density lipoprotein receptors on BBB endothelial cells surfaces, resulting in their endocytosis into the endothelial cells and subsequent transport through the BBB and into the brain [14]. In a PD mouse model, NPs coated with PS80 successfully passed through the BBB and released the therapeutic resveratrol causing neuroprotective effects and enhanced olfactory discrimination and social recognition [14].

In addition to being able to pass the BBB, the unique properties of some NPs can overcome other barriers faced by conventional therapeutics designed for PD. Through encapsulation, NPs can mask any undesirable physicochemical properties of a therapeutic agent, while imparting beneficial properties though the functionalisation of the NP surface. For example, NPs can be engineered to improve drug biocompatibility, solubility, blood-circulation time, facilitate co-treatment, and enable the targeted and controlled release of a drug that enhances its therapeutic efficacy [15]. Additionally, the ability to encapsulate drugs inside an NP can protect and stabilise a drug while also limiting any direct interaction with the body, thereby mitigating any toxicity or adverse side-effects in patients [15]. The benefits of NP surface functionalisation are demonstrated through NPs coated with polyethylene glycol (PEG) [16]. PEGylation imparts “stealth” properties by preventing the formation of a protein corona around the NP, thereby making the NP unrecognisable to the immune system, resulting in prolonged circulation times and reduced clearance [16]. NPs are highly diverse and can be developed from a wide-range of materials, including lipids (liposomes), surfactants (micelles), metals and metal oxides (gold, silver, and iron oxide), polymers (poly(lactic-co-glycolic acid) NPs) [PLGA]), carbon (carbon nanotubes), semiconductors (quantum dots) and proteins (virus-like particles) [17]. Each class of NP exhibits significantly novel and distinct physicochemical (e.g. size, shape, composition, surface chemistry and charge), and biological

properties (e.g. bioavailability, cytotoxicity, biodegradability) that determines its optimal application.

1.3 Current Progress into Nanoparticle-based Treatments of Parkinson's Disease

Over the past decade, an increasing number of studies have investigated the potential of various NPs in repurposing or improving existing drugs to alleviate PD symptoms. Hawthorne et al. [18] provided a systematic review of studies that utilised NPs as drug delivery vehicles for PD therapeutics between 2009-2015. This section describes the more recent studies of NPs in PD drug delivery which are also summarised in Table 1.

L-DOPA

As outlined above, the loss of dopaminergic neurons and the subsequent decrease of dopamine concentration in the brain results in the motor symptoms of PD [4]. As dopamine is highly hydrophobic and unable to pass the BBB, its metabolic precursor L-DOPA is often utilised as a therapeutic for PD. L-DOPA actively traverses the BBB via the large amino acid transporter (LAT)-1 and is converted into dopamine by DOPA decarboxylase, increasing dopamine concentrations in the brain and relieving motor symptoms [8]. However, despite being the most commonly used drug to treat PD, L-DOPA has been associated with severe side-effects, including anomalous involuntary movements known as L-DOPA-induced dyskinesia [8]. L-DOPA-induced dyskinesia may be caused by the intermittent change of L-DOPA concentration in the blood from variable gastrointestinal absorption upon use of orally administered drugs [8]. Therefore, strategies that facilitate the controlled and continuous delivery of L-DOPA could potentially alleviate these side-effects.

The controlled delivery of L-DOPA was investigated using carboxylated single walled carbon nanotubes (SWCNT) coated with biopolymers to confer aqueous solubility and biocompatibility to the NP [19]. *In vitro* drug release profiles showed the coatings Tween 20, Tween 80, chitosan, and polyethylene glycol facilitated a more continuous release of L-DOPA compared to uncoated SWCNTs [19]. Additionally, cellular viability assays with the mouse embryonic fibroblast 3T3 cell line found the coatings improved the biocompatibility of L-DOPA loaded SWCNTs by 34-41% compared to uncoated SWCNTs [19]. McDonagh et al. [20] also explored the gradual release of L-DOPA in conjunction with manganese oxide NPs as an MRI

contrast agent for dual diagnostic and therapeutic use. As manganese ions are analogous with calcium ions, manganese oxide NPs could exploit the voltage-gated calcium channel to enter neurons [20]. The study found that both manganese ions and L-DOPA were gradually released during the degradation of the NPs in *in vivo* and *ex vivo* pig eye models [20]. However, studies using neuronal cells are required to evaluate the NP's suitability for use in PD. In another report, a layered double hydroxides (LDHs), constructed from Tween-80 coated zinc-aluminium, was loaded with L-DOPA and administered into rats to investigate its biodistribution and toxicity [21]. Atomic absorption spectroscopy was used to analyse zinc concentrations in tissue samples and showed that the L-DOPA-loaded LDHs were able to enter the brain. In addition, non-treated and LDH-L-DOPA treated rats showed no difference in body weight or biochemical and histopathological changes, indicating no apparent toxic effects of the LDHs at 2000 mg/kg [21]. However, this study did not investigate the therapeutic effects of the L-DOPA loaded LDHs. Gonzales-Carter et al. [22] functionalised multi-branched nanoflower-like gold nanoparticles (AuNFs) with L-DOPA to bind with its transporter LAT-1. An *in vitro* model of human BBB and brain endothelial monolayers isolated from rats indicated successful passage of L-DOPA through the BBB determined by high-resolution transmission electron microscopy, and the absence of microglial activation demonstrated the AuNFs anti-inflammatory effects [22]. The study also demonstrated the influence shape has on an NPs efficacy, as the multi-branched design provided an increased surface area compared to spherical counterparts and led to enhanced drug loading volume [22].

Another complication encountered in the use of L-DOPA as a therapeutic is a large amount is converted into dopamine by DOPA decarboxylase via first-pass metabolism in the bloodstream prior to reaching its site-of-action in the brain [23]. Consequently, to ensure efficacy, high doses of L-DOPA are administered to patients, often resulting in adverse side-effects such as nausea and orthostatic hypotension [23]. Co-administration of a DOPA decarboxylase inhibitor, such as carbidopa or benserazide, can improve the pharmacokinetics of L-DOPA, thereby limiting L-DOPA dosage and reducing the potential side-effects from high dosing [23]. Sintov et al. [24] designed a self-assembling nanomicellar system to transdermally deliver L-DOPA and carbidopa. L-DOPA has limited permeability through the skin due to being poorly soluble in water; therefore, micelles were utilised to solubilise and transport L-DOPA. *In vivo* studies were conducted through the application of patches containing the L-DOPA/carbidopa loaded micelles to the skin of rabbits. Liquid

chromatography-tandem mass spectrometry analysis of blood plasma showed peaks between 0.2-0.4 μg/mL of both L-DOPA and carbidopa, indicating its successful permeation through the skin [24]. However, the study did not determine whether the drugs penetrated into the brain, or if any therapeutic outcomes were achieved. In an alternative approach, Sharma et al. [25] investigated eliminating the need for an inhibitor and minimising peripheral L-DOPA conversion by delivering NPs loaded with only L-DOPA directly to the brain intranasally, bypassing the BBB. Chitosan displays multiple characteristics desirable in an NP, including being mucoadhesive, which is beneficial for nasal delivery, and it increases the permeability of epithelium layers by opening tight junctions which are present in the nasal epithelium [25]. Chitosan NPs containing L-DOPA (CNL) were inserted into thermo-reversible gel (Pluronic PF127) (CNLP) for ease of administration and to prolong residence time for drug absorption in the nasal mucosa. Intranasal administration of this formulation into rats demonstrated sustained release of L-DOPA and drug recovery in the brain of 74.7 $\pm$ 2.27% for CNLs and 25.99 $\pm$ 2.21% in CNLPs determined by spectroscopic analysis of brain plasma [25].

As demonstrated by the above examples, functionalised NPs could provide mechanisms to alleviate current barriers in the use of L-DOPA. NPs could help avoid L-DOPA-induced dyskinesia associated with fluctuating L-DOPA concentrations in the body by facilitating the continuous and controlled administration of L-DOPA. Additionally, NPs could be used to allow co-administration of DOPA decarboxylase inhibitors to limit the degradation of L-DOPA and improve its bioavailability, thereby reducing the need for high dosages linked to adverse side-effects.

Dopamine Agonists

Dopamine agonists (DAs) are drugs that act on PD symptoms by simulating dopamine to activate its receptors and help restore dopaminergic signalling in PD patients [26]. DAs are less effective than L-DOPA but are often employed as an early PD treatment to delay L-DOPA treatment, or used in conjunction with lower amounts of L-DOPA to minimise L-DOPA side-effects [26]. Ropinirole is a commonly used DA that is orally administered in tablet form. However, this delivery route makes Ropinirole susceptible to first-pass metabolism within the liver, and consequently the majority of the drug does not enter the brain [27]. NPs have,

therefore, been explored as a mechanism to allow alternative administration routes to deliver Ropinirole to the brain and thus increase its bioavailability.

Barcia et al. [28] created a biodegradable poly (D,L-lactide-co-glycolide) (PLGA) NP designed to facilitate targeted brain delivery and sustained release of Ropinirole. The Ropinirole-loaded PLGA NPs were injected into the peritoneum of rotenone-induced rat models of PD, and the treated rats displayed improved cognitive behaviour and motor coordination when compared to non-treated rats. Brain histology and immunochemistry results indicated that treatment with Ropinirole-PLGA NPs reduced PD-like symptoms in the rats by reducing cell death in both the substantia nigra and astrogliosis [28]. The targeted delivery of Ropinirole to the brain was similarly investigated with polysorbate 80 coated chitosan NPs designed to increase brain uptake of the drug [27]. Polysorbate 80 coating causes the adsorption of apolipoproteins from the blood onto the surface of NPs, facilitating the binding of the NPs to lipoprotein receptors on the BBB surface and enabling receptor-mediated endocytosis passage of NPs into and subsequently through the BBB [27]. Rats treated with polysorbate 80 coated NPs showed a higher brain to blood ratio of Ropinirole than those treated with uncoated NPs or free Ropinirole. These results indicate that the coated NPs were able to pass the BBB with high efficiency, targeting Ropinirole to the brain [27].

Rotigotine is another DA with limited effectiveness because of its short half-life and low bioavailability [29]. Rotigotine is administered with a transdermal patch to improve its bioavailability by controlled-release, but adverse skin reactions at the site of application may be experienced [26]. Bi et al. [30] designed PEGylated PLGA NPs that demonstrated high biocompatibility, and long blood circulation times. The NP was functionalised with surface lactoferrin ligands, and then loaded with Rotigotine (Lf-R-NPs) and administered intranasally into mice [30]. Preliminary studies showed Rotigotine alone was cytotoxic to cells, but when loaded into the NP, its physicochemical properties were concealed, and its cytotoxicity was reduced. Functionalisation with lactoferrin resulted in enhanced cellular uptake and accumulation to the target area of the brain in the mice studies [30]. A subsequent study from the same research group focused on the distribution and neuroprotective properties of the Lf-R-NPs, and explored whether the functionalisation with lactoferrin improves delivery in 6-hydroxydopamine-induced PD rat models [31]. Liquid extraction surface analysis with tandem mass spectrometry found a higher amount of Rotigotine in the brains of rats treated with Lf-

R-NPs compared to PLGA NPs without lactoferrin, indicating the high expression of lactoferrin receptors on the surface of neurons and brain endothelial cells enabled increased targeted passage through the BBB. Additionally, neuroprotective effects were observed as Lf-R-NP treated rats demonstrated decreased contralateral rotations compared to non-treated rats, along with a reduction in dopaminergic neuron loss visualised via immunohistochemistry [31].

These studies demonstrate the potential of NPs in protecting DA drugs from first-pass metabolism and facilitating targeted delivery to the brain, thereby enhancing drug bioavailability and efficacy.

Monoamine Oxidase Type B Inhibitors

Monoamine oxidase type B (MAO-B) inhibitors are another class of drugs used in the treatment of PD. Similar to DAs, they are less effective than L-DOPA and tend to be used as an initial treatment option or as an adjunct to L-DOPA treatment [32]. MAO-B inhibitors elicit anti-Parkinsonian effects by irreversibly inhibiting the MAO-B enzyme from metabolising dopamine, thereby maintaining the existing dopaminergic activity in the brain [32]. The MAO-B inhibitor Rasagiline is available as an orally administered drug, but this route of administration has been linked to gastrointestinal side effects, a short half-life, and a bioavailability of only 36% due to extensive first-pass metabolism in the liver [32].

Ahmad [33] developed Rasagiline-encapsulated chitosan-coated PLGA NPs designed for intranasal delivery. Chitosan was selected for its high mucoadhesive potential and ability for sustained drug release. Following nasal administration, high-performance liquid chromatography-tandem mass-spectroscopy (LC-MS/MS) revealed enhanced Rasagiline accumulation inside rat brains, indicating successful brain targeting of the chitosan-coated PLGA NP [33]. As an alternative approach to achieve MAO-B inhibition, encapsulation inside a PLGA NP could mediate permeation of the reversible and selective MAO-B inhibitor coumarin C75 directly through the BBB, rather than bypassing the BBB intranasally [34]. The BBB efflux transporter P-glycoprotein (P-gp) was found to prevent lone coumarin C75 passage through the BBB. The researchers found that by functionalising the surface of the PLGA NP with PEGylated surfactant P188 the P-gb mediated efflux was inhibited, and the coumarin C75 loaded NPs were able to successfully permeate through a cellular *in vitro* BBB model determined by high performance liquid chromatography [34]. In addition, coumarin C75 alone was found to be cytotoxic to cell lines, but when loaded into PLGA NPs it displayed no

cytotoxic effects [34]. This study demonstrated the potential for the NP facilitated delivery of a MAO-B inhibitor into the brain, but further studies are required to evaluate its effectiveness on the treatment of PD.

Table 1. *Recent nanoparticle-based delivery systems developed for the potential treatment of PD*

Pathological Mechanism Targeted	**Nanoparticle**	**Drug/therapy**	**Outcome**	**Models tested**		**Refs**
				In vitro	***In vivo***	
Increase of dopamine concentration	Gold	L-DOPA	Successful uptake into the brain and non-inflammatory effects in *in vitro* human BBB cell models.	✓		[22]
	Micelle	L-DOPA & carbidopa	Permeation into the bloodstream transdermally in *in vivo* rabbit studies.		✓	[24]
	Carbon nanotube	L-DOPA	NP system achieved sustained drug release pattern and enhanced bioavailability in an *in vitro* cell model.	✓		[19]
	Manganese oxide	L-DOPA	NP gradually degraded and released L-DOPA *ex vivo.*	✓		[20]
	Zinc & aluminium layered double hydroxide	L-DOPA	Release of L-DOPA in the brain with no apparent toxic effects in rat models.		✓	[21]
	Carbon nanotube	L-DOPA & benserazide	Predicted to display a high drug loading efficiency via computational modelling.			[35]
	Chitosan	L-DOPA	Sustained release and increased percentage of L-DOPA observed in the brain of rat models.	✓	✓	[25]
Dopamine agonists	PLGA	Ropinirole	Reversed PD-like symptoms of neurodegeneration in rat models.	✓	✓	[28]
	Chitosan	Ropinirole	A higher brain to blood ratio of encapsulated Ropinirole compared to free Ropinirole was found in rat models.	✓	✓	[27]
	PLGA	Rotigotine	Enhanced cellular uptake and targeted delivery in mice models.	✓	✓	[30]
	PLGA	Rotigotine	NP system showed high targeting capability and efficacy, exhibiting neuroprotective effects in rat models.		✓	[31]
Monoamine oxidase type B inhibition	Chitosan	Rasagiline	NPs enhanced Rasagiline bioavailability in the brains of rat models, indicating successful brain targeting of the NP.	✓	✓	[33]
	PLGA	Coumarin C7	Successfully permeated the BBB and displayed no cytotoxic effects in *in vitro* cell models.	✓		[34]
	Poly(lactide)	Resveratrol	Demonstrated neuroprotective effects and improved cognitive effects in mouse models.	✓	✓	[14]

1.4 Nanoparticles as Disease-Modifying Agents in PD

As outlined above, current PD medications only alleviate its symptoms and do not alter its causative mechanisms. As the progression of α-synuclein throughout the brain is linked to the PD progression, targeting this protein could provide a disease modifying treatment. A number of strategies that target α-synuclein are currently in preclinical development [36]. However, new approaches that explore the potential of nanoparticles (NPs) to target α-synuclein are still in their infancy, and primarily focus on reducing the expression of the α-synuclein, or physically interfering with its fibrillation formation [37-41].

Virus-like particles (VLPs) are protein-based nanoparticles, and the lentiviral vector (LV) VLP was investigated as a vehicle to deliver the genes encoding the serine protease neurosin into neuronal cells [39]. Neurosin degrades both monomeric and oligomeric forms of α-synuclein, and neurosin levels were found to be decreased in the brains of both patients with PD and dementia with Lewy bodies (DLB), and α-synuclein transgenic mouse models [39]. The LVs were delivered into B103 neuronal cells and following subsequent expression of neurosin, α-synuclein was degraded and the cells showed a reduction in wild-type α-synuclein accumulation. In contrast, no effect was observed on A53T mutated α-synuclein which is associated with familial PD. The LVs were then delivered into α-synuclein transgenic mice. Following treatment, brain sections were isolated and the MAP2 marker for neuronal damage was assessed via immunohistochemistry. Both a reduction in α-synuclein accumulation and α-synuclein accumulation associated neuronal damage was observed in wild-type α-synuclein transgenic mice, but similar to the *in vitro* studies, no effect was found in the A53T mutated mice. It is possible the A53T α-synuclein displays an alternative protein fold that protects degradation from the protease, and therefore this system is limited as it may not be effective for alternative pathogenic forms of α-synuclein [39].

Synthetic NPs have also been evaluated as gene delivery vehicles to target α-synuclein. For example, Niu et al. [38] developed magnetic Fe_3O_4 NPs functionalised with oleic acid (290 nm) designed to deliver short hairpin RNA (shRNA) and supress neuronal expression of the α-synuclein encoding gene SNCA. By supressing the overexpression of α-synuclein, toxic aggregations could be reduced. The NP was further functionalised with *N*-isopropylacrylamide and acrylic acid (NIPAm-AA) polymer material which displays sensitivity

to temperature and pH. Degenerative apoptosis occurs in the brains of PD patients and as apoptotic cells display a lower pH than healthy tissue, this was utilised to facilitate targeted release. Nerve growth factor (NGF) was also added to the NP to facilitate receptor-mediated endocytosis into PC-12 cells. *In vivo* mouse locomotion studies found a higher activity in mice treated with the NPs compared to mice without, and immunohistochemical staining and western blots indicated a down-regulation of α-synuclein and suppression of further apoptosis in NP-treated brain tissue [38]. Similarly, another study investigated the use of polyethylenimine (PEI) NPs to protect and intracellularly deliver small interfering RNA (siRNA) to reduce the expression of SNCA [37]. Thy1-aSyn mice overexpressing SNCA as a PD model were injected with 0.75 μg of siRNA-loaded PEI NPs and after 5 days a ~50% reduction in wild-type α-synuclein was found in the mice striatum, medial septum, and cortex. Additionally, no toxicity was observed [37].

As an alternative to gene therapy, the application of NPs to directly prevent the formation of pathogenic α-synuclein fibrils has been investigated. Taebnia et al. [40] loaded amine-functionalised mesoporous silica nanoparticles to load curcumin (CUR-AAS-MSNPs). Curcumin has demonstrated inhibitive effects of the formation of α-synuclein oligomers [40]. Circular dichroism spectra revealed that α-synuclein, in the absence of CUR-AAS-MSNPs, displayed spectra showing the formation of β-sheets, which is indicative of pathological fibril formation. However, upon addition of CUR-AAS-MSNPs, α-synuclein was adsorbed electrostatically to the surface of the CUR-AAS-MSNPs and retained its disordered monomeric structure (i.e. no fibril formation). Cytotoxicity studies indicated that PC-12 neuronal cells retained 85% viability at ≤100 ug/mL of CUR-AAS-MSNPs, showcasing the NPs' biocompatibility [40]. In a similar approach, wild-type α-synuclein was found to strongly adsorb electrostatically to gold NPs (20 nm and 90 nm), maintaining its native conformation and preventing aggregation [41]. Whilst these approaches prevented the fibrillation of monomeric α-synuclein, they are not specifically targeted to α-synuclein and their efficacy *in vivo* remain unknown.

1.5 Future Potential of NPs in the Treatment of Parkinson's Disease

Functionalised NPs present a promising approach to enhance drug efficacy in PD. Whether designed to circumvent first-pass metabolism and the BBB by entering the brain intranasally, or to pass the barriers of the BBB directly, outer functionalisation of NPs can impart the physicochemical properties required for targeted brain delivery and increase drug bioavailability in the brain. As of 2016, 51 NP therapeutics had been FDA-approved and 77 NP therapeutics were undergoing clinical trials for a range of diseases, primarily cancer [42]. However, no NP-based therapeutic designed for treatment of PD has successfully reached clinical trials to date. A significant limiting factor of the progression to clinical trials is the potentially harmful accumulation of NP systems in off-target healthy tissue [13]. The development of NP systems that can be remotely triggered to release drugs solely at the brain, and, furthermore, target particular brain cells, will contribute to clinical translation [13]. Van der Munnik et al. [43] identified poor comparability between studies in the field as an obstacle to understanding the mechanism of action displayed by NP systems. Studies into NP therapeutics tend to vary in conditions and comprise isolated NP system/target interactions. However, focusing on a single system instead could improve understanding of its mechanism of action, and, hence, its progression to clinical translation [43]. Additionally, the absence of supporting experimental observations with theoretical analysis is a limitation of many NP studies [43]. The incorporation of computational modelling could link isolated experimental observations and enhance the understanding of NP mechanisms [43]. If these limitations can be addressed, NPs hold great potential as therapeutics for currently incurable diseases, like PD.

To overcome the limitations of synthetic NPs, such as adverse off-target effects, there is a growing interest in alternative NPs derived from nature, including protein-based NPs (PNPs), due to their biocompatibility, low toxicity, and enhanced engineerability.

1.6 Encapsulin Protein Nanocages

Encapsulin protein nanocages are an exciting new class of PNPs found in bacteria and archaea that precisely self-assemble from identical protein subunits into hollow icosahedral capsid-like nanocompartments [15]. Being biologically derived, encapsulins have the important

benefits of being soluble, non-toxic, monodisperse, and *in vivo* studies in rats demonstrated their biocompatibility in the brain [44, 45]. Encapsulins can be genetically engineered internally, externally, and in-between subunits. This allows site-specific functionalisation and therefore enhanced control over their physicochemical properties. At present, no studies have investigated encapsulin's ability to cross the BBB, however, their high engineerability makes them well suited to be functionalised with moieties such as those described above to facilitate passage. Additionally, other PNPs have demonstrated ability to cross the BBB, such as lactoferrin PNPs [46]. Due to the enhanced control over encapsulin's properties, they have recently attracted attention as potential drug delivery vehicles [15, 44]. They exist in a variety of sizes (18-42 nm in diameter) with different triangulation numbers (facet numbers per icosahedral face (T)); T = 1 (60 subunits, 18-24 nm; e.g. *Thermotoga maritima* encapsulin (TM)); T = 3 (180 subunits, 32-38 nm, e.g. *Myxococcus xanthus* encapsulin (MX)), T = 4 (240 subunits, 42 nm, e.g. *Quasibacillus thermotolerans* encapsulin (QT)) [47-49].

Encapsulins display a unique loading mechanism whereby nanocages selectively package native cargo proteins that display a C-terminal 'Encapsulation signal' (ESig) peptide sequence [50]. Genetically tagging foreign cargo proteins with ESigs leads to their targeted loading into encapsulin, providing an highly modular platform for protein encapsulation [50]. As shown in Figure 2, the selective loading of foreign proteins into encapsulins can be achieved via two methods: (i) *in vivo* (during self-assembly), by co-expressing encapsulin and an ESig-tagged protein in a heterologous host (e.g. *Escherichia coli*); or (ii) *in vitro* (during reassembly) by disassembling empty encapsulin under denaturing conditions and then reassembling it by dilution to normal conditions in the presence of ESig-tagged cargo [50]. To date, my research group at Macquarie University (Sydney, Australia) have employed both strategies to load a range of ESig-tagged proteins into the encapsulin from the bacterium *T. maritima* (Fig. 2).

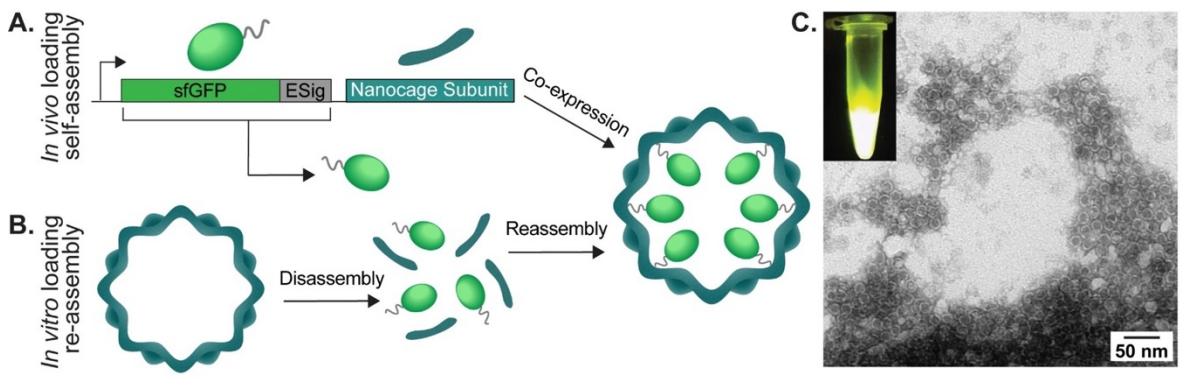

Figure 2: Diagram showing **(A)** *in vivo* loading of ESig-tagged superfolder green fluorescent protein (sfGFP) into encapsulin during its self-assembly (inside *E. coli*). **(B)** *in vitro* loading of CLP-tagged sfGFP into encapsulin during its re-assembly. **(C)** Transmission electron microscope image of purified sfGFP-loaded encapsulin (~25 nm). Inset is a photograph of the green fluorescence from the encapsulated sfGFP under blue light excitation. *Care et al. unpublished data.*

1.7 Scope of This Thesis

Encapsulins' unique self-assembly, cargo-loading mechanisms and engineerability makes them an ideal NP platform to selectively 'capture' α-synuclein. Directly capturing α-synuclein from the extracellular space between neurons could prevent its transmission and therefore halt or slow the pathological spread of PD throughout the brain (Figure 3).

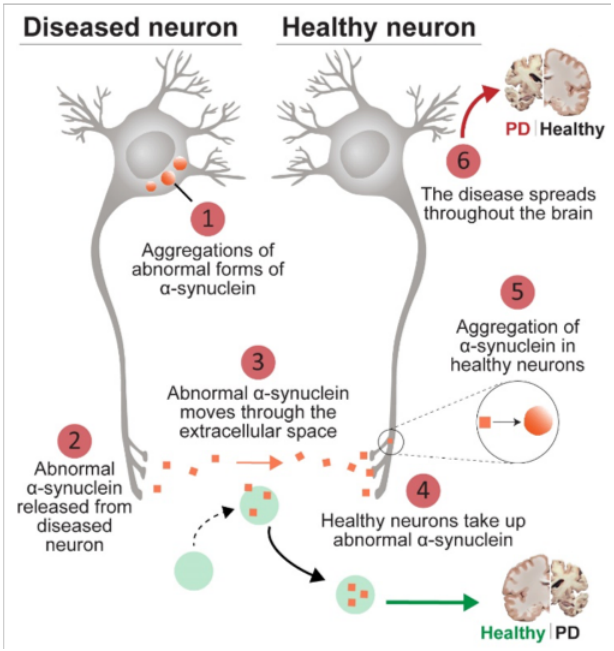

Figure 3: Proposed mechanism of capture to disrupt the spread of *α-syn* (orange squares) from diseased to unaffected neurons (steps 1-6, red). We propose using a novel nanocage system (depicted in green) to capture this extracellular α-syn, preventing its transmission.

The overarching aim of this Master of Research (MRes) thesis was to investigate the potential of a novel encapsulin nanocage system for the targeted capture of α-synuclein, providing a stepping-stone towards a new technology that can halt α-synuclein transmission and PD progression.

In pursuit of this goal, our objectives were as follows:

i) Characterisation of the biomechanical mechanisms and physicochemical factors underlying encapsulins disassembly/reassembly process.

ii) Evaluation of the ability for encapsulin cargo-loading system to be re-programmed to capture foreign unmodified proteins.

iii) Application of encapsulins to selectively capture α-synuclein *in vitro.*

Chapter 2: Materials and Methods

2.1 Production and Purification of Protein Components

Molecular Cloning of Constructs

All inserts were codon optimised for expression in *Escherichia coli* and custom synthesised as gBlock Gene Fragments (Integrated DNA Technologies). Encapsulins (Enc) from *Thermotoga maritima (TM)*, *Myxococcus xanthus (MX)* and *Quasibacillus thermotolerans (QT)* were each synthesised with flanking restriction sites (*Nco*I/*Bam*HI). Nanobodies were synthesised with either a 30 or 15 aa C-terminal ESig (LFTDKPITEIEEETSGGSENTGGDLGIRKL or GGSENTGGDLGIRKL, respectively) and flanking restriction sites (*NdeI/BglII*). sfGFP was synthesized with flanking restriction sites (*AseI/BglII*). For gene expression in *E. coli*, TM_Enc was cloned into pETDuet-1 (Novagen, Merck, USA) plasmids, MX_Enc and QT_Enc were cloned into pACYC-Duet-1 (Novagen, Merck, USA) plasmids, and all nanobodies were cloned into pET-22b (+) (Novagen, Merck, USA) plasmids (Table 1).

Table 2. *Expression plasmids constructed for this study.*

Protein	**Description**	**Plasmid**	**Selection antibiotic**	**Uniprot or Protein database (PDB) number**
TM_Enc	Encapsulin isolated from *Thermotoga maritima*	pETDuet-1	Carbenicillin	Q9WZP3
MX_Enc	Encapsulin isolated from *Myxococcus xanthus*	pACYC-Duet-1	Chloramphenicol	Q1D6H4
QT_Enc	Encapsulin isolated from *Quasibacillus thermotolerans*	pACYC-Duet-1	Chloramphenicol	A0A0F5HPP7
*sf*GFP	Superfolder green fluorescent protein. Includes His-TEV sequence	pET-duet-1 (+)	Carbenicillin	P42212
GFPnb-ESig	Anti-*sf*GFP nanobody tagged with 30 aa ESig. Contains pelB signal sequence	pET-22b (+)	Carbenicillin	3OGO (PDB)
GFPnb-ESig$_T$	Anti-*sf*GFP nanobody tagged with truncated 15 aa ESig. Contains pelB signal sequence	pET-22b (+)	Carbenicillin	3OGO (PDB)
Syn2nb-ESig	Anti-α-synuclein nanobody tagged with 30 aa ESig. Includes His-TEV sequence. Contains pelB signal sequence	pET-22b (+)	Carbenicillin	2X6M (PDB)
Syn2nb-ESig$_T$	Anti-α-synuclein nanobody tagged with truncated 15 aa ESig. Contains pelB signal sequence	pET-22b (+)	Carbenicillin	2X6M

Recombinant Protein Production in E. coli

E. coli BL21 (DE3) cells (New England Biolabs) were used for recombinant protein expression (New England Biolabs, USA). Herein, cells were transformed with the appropriate plasmids, and the resulting transformants were selected on Luria–Bertani (LB) agar supplemented with the relevant antibiotic (100 μg/mL of carbenicillin or 50 μg/mL of chloramphenicol) (see Table. 1). Plates were incubated overnight at 37°C until colonies grew. A starter culture (1 colony in 5 mL LB media supplemented with the relevant antibiotic) was grown for 16 h at 37°C and used to inoculate LB media (500 mL) supplemented with the relevant antibiotic and incubated at 37°C/200-250 rpm until reaching an OD_{600} reading of 0.5-0.6 for encapsulin-producing strains, and 0.6-0.9 for *sf*GFP and nanobody-producing strains. Protein synthesis was then induced by the addition of isopropyl-β-d-thiogalactopyranoside (IPTG) to a final concentration of 0.1 mM. Induced cultures were incubated at 37°C/200-250 rpm for 4 h and then harvested via centrifugation (8,000 xg, 4°C, 15 min) with the resulting cell pellets stored at -20°C until further use.

Recombinant Protein Extraction and Isolation

Cell pellets from encapsulin-producing cultures were thawed and resuspended in 5 mL of lysis buffer (50 mM 4-(2-hydroxyethyl)-1-piperazineethanesulfonic acid (HEPES) buffer, pH 7.4 and Benzonase® nuclease 10 U/mL). Cells were lysed by three rounds of passage through a French Pressure cell at 1000 psi and centrifuged (8,000 xg, 4°C, 15 min). Supernatant containing soluble protein was heat treated in a water bath at 65°C for 15 min before centrifugation (10,000 xg, 4°C, 10 min). Protein precipitation was initiated by adding PEG8000 (0.5 g/5 mL) and NaCl (0.1 g/5 mL) to the supernatant followed by incubation on ice (30 min). Sample was centrifuged (10,000 xg, 4°C, 10 min) and pellet was resuspended in 2.5 mL of HEPES buffer (50 mM, pH 7.4) and filtered through a 0.22 μm syringe filter.

Cell pellets from cultures producing *sf*GFP, GFPnb-ESig, or GFPnb-$ESig_T$ were resuspended in 1 mL HEPES buffer (50 mM, pH 7.4) and transferred to BeadBug™ tubes (Sigma-Aldrich) containing silica beads for lysis via bead beating. A BeadBug Microtube Homogeniser (Pathtech) was run 3x for 15 s at 4000 rpm, with samples cooled on ice between runs. Samples were centrifuged (500 xg, 4°C, 2 min), and the supernatant was transferred to new tubes before being centrifuged again to isolate soluble protein (13,000 xg, 4°C, 30 min).

Due to the insolubility of Syn2nb-ESig and Syn2nb-ESig$_T$ nanobodies, they were expressed with PelB leader sequences to facilitate periplasmic localisation and allow periplasmic extraction via osmotic shock as described by Broisat et al. [51]. Briefly, pellets from a 0.5 L cell culture were resuspended in 6 mL TES buffer (0.2 M Tris-HCl pH 8.0, 0.5 mM EDTA, 0.5 M sucrose) and inverted on a rotary shaker in a 4°C room for 1 h, then fourfold-diluted TES (12 mL) was added to the cell suspension and inverted for a further 2 h. The suspension was then centrifuged (13 000 xg, 4°C, 30 min) and supernatant containing soluble proteins was collected.

Protein Purification

Encapsulins were purified via size exclusion chromatography (SEC) using a HiPrep 26/60 Sephacryl S-500 HR column (GE Healthcare) equilibrated with equilibration buffer (50 mM HEPES, pH 7.4, 0.22 μm filtrated and degassed). Cell lysate was passed through and eluted with 1.5 column volumes (CV) of HEPES (50 mM, pH 7.4) into fractions at 1.3 mL/min (0.15 MPa) operating on an ÄKTA Start system (GE Healthcare) at 4°C. Fractions containing encapsulin were identified via SDS-PAGE and subject to further purification via anion-exchange chromatography. A Q HiPrep 16/10 column was equilibrated with 2 CV of Buffer A (HEPES, 50 mM, pH 7.4), 3 CV of Buffer B (HEPES, 50 mM, pH 7, 1 M NaCl), followed by 5 CV of Buffer A. Lysate was passed through the column operating on an ÄKTA Start (GE Healthcare) at room temperature at 3 mL/min, and unbound proteins were washed with 3 CV of Buffer A. Elution was done with a linear gradient of 0-30% Buffer B (3 CV), 30% Buffer B (4 CV), a linear gradient of 30-100% Buffer B (10 CV), and 100% Buffer B (4 CV). Fractions containing encapsulin were identified via SDS-PAGE and buffer exchanged into HEPES (50 mM, pH 7) using 100 kDa spin columns (Amplicon) at 7,000 xg for 8 min (4°C), filtered through a 0.22 μm syringe filter and finally stored at -20°C.

Syn2nb-ESig and *sf*GFP contained His-TEV tags and were therefore subject to His-tag purification. For Syn2nb-ESig, a 1 mL HisTrap HP column (GE Healthcare) was equilibrated with Native wash buffer (50 mM NaH_2PO_4 pH 8, 300 mM NaCl, and 20 mM Imidazole) and lysate was passed through at 1 mL/min (0.3 MPa) operating on an ÄKTA Start system (GE Healthcare) at room temperature. The column was washed with 10 CV of Native wash buffer and His-tagged protein was eluted over a 10 CV gradient elution to 100% Elution buffer (50

mM NaH_2PO_4 pH 8, 300 mM NaCl, and 500 mM Imidazole). Fractions containing Syn2nb-ESig were identified via SDS-PAGE and pooled. ProTEV Plus Protease (Promega) was used to cleave at the TEV site and remove the His-tag. As per manufacturer's instructions, the TEV protease was added to the protein sample and incubated for 1 h at 30°C (600 rpm) and then kept at 4°C overnight. Cleaved His-tag and protease were removed from the digested sample using a 1 mL HisTrap HP column (GE Healthcare) equilibrated with Native wash buffer. Herein, the flowthrough containing the untagged protein was collected, with any unwanted His-tagged protein (undigested) later eluted via a stepwise elution to 100% Elution buffer.

His-TEV-tagged *sf*GFP was purified using a Ni-NTA Fast Start Kit (QIAGEN) following the manufacturer's instructions. ProTEV Plus Protease (Promega) was used for TEV cleavage as per manufacturer's instructions, and His-tag and protease removal were performed using the Ni-NTA Fast Start Kit (QIAGEN). His-tag removal was confirmed via SDS-PAGE and both Syn2nb-ESig and *sf*GFP were buffer exchanged into HEPES (50 mM, pH 7.4) using 3 kDa spin columns (Amplicon) and stored at 4°C for subsequent use (or -20°C for longer storage).
GFPnb-ESig and GFPnb-$ESig_T$ soluble protein was partially purified from cell lysates via heat treatment at 75°C for 15 min.

2.2 Protein Analysis Methods

Protein Gel Electrophoresis and Protein Quantification

Protein samples were denatured, separated, and visualised using sodium dodecyl sulfate polyacrylamide gel electrophoresis (SDS-PAGE), with molecular weights compared with a commercial protein ladder (Precision Plus Protein, BioRad). Protein samples were mixed in a 1:1 ratio with 2x loading dye (0.125 M Tris-HCl pH 6.8, 25% Glycerol, 0.01% bromophenol blue, 2% SDS) and heated at 99°C for 10 min at 300 rpm. Electrophoresis was performed at 200 V for 30 min on a 4-20% polyacrylamide gel (Mini-PROTEAN® TGX™, BioRad) in SDS running buffer (25 mM Tris, 192 mM glycine, 1% (w/v) SDS, pH 8.3). Gels were fixed via incubation in boiling water for 2 min three times followed by Coomassie staining solution (0.08% Coomassie Brilliant Blue G-250, 3.5 mM HCl) for 10 min, and de-stained in water overnight.

Encapsulin assembly (with and without cargo-loading) and 'nanobody + target' binding was visualised via Native-PAGE (non-denaturing). Protein samples were mixed in a

1:4 ratio with 4X Native-PAGE loading dye (0.125 M Tris-HCl pH 6.8, 40% Glycerol, 0.01% bromophenol blue) and electrophoresis was performed at 200 V for 120 min on a 4-20% polyacrylamide gel (Mini-PROTEAN® TGX™, BioRad) in Native-PAGE running buffer (25 mM Tris, 192 mM glycine, pH 8.3). Gels were imaged to detect fluorescence using a Typhoon Trio variable-mode imager system (GE Healthcare). The *sf*GFP and HiLyte™ Fluor 488 labelled recombinant human α-synuclein (AnaSpec) proteins were excited at 532 nm and a 520 nm band-pass emission filter was used, and the IRDye 680RD Goat anti-Rabbit secondary antibody (Li-Cor) was excited at 633 nm with a 670 nm band-pass emission filter. Gels were then fixed and stained as described above.

Protein concentration was either determined by measuring the A_{280} of 2 μL on a NanoDrop 2000 Spectrophotometer instrument (Thermo Scientific), or via mid-infrared spectroscopy on a Direct Detect® FTIR spectrometer (Sigma-Aldrich).

Characterisation of In Vitro Disassembly/Reassembly of Encapsulin

In vitro disassembly of encapsulin via denaturant was done by the addition of guanidine hydrochloride (GuHCl) diluted with HEPES (50 mM, pH 7.4) to the desired molarity (1-7 M). Disassembly of encapsulin *in vitro* via pH alteration (pH 3-13) was done by adding HEPES (50 mM, pH 7.4) supplemented with varying concentrations of hydrochloric acid or sodium hydroxide until the desired pH was reached (confirmed by pH strips (Sigma)). In both disassembly methods, dithiothreitol (DTT) was added to the encapsulin sample to a final concentration of 1 mM, incubated for 1 h, and centrifuged at 10 000 g for 5 min. Reassembly was initiated by diluting the disassembled solution 1:10 with HEPES (50 mM, pH 7.4) buffer and incubation at room temperature for at least 16 h. Reassembled solutions were centrifuged for 10 min at 10,000xg to remove any aggregated proteins. The resulting supernatant was concentrated by centrifugation through a 100 kDa spin column (Amplicon) for 2.5 min at 5,000 xg. For *in vitro* loading of *sf*GFP-CLP, 0.1 μM of encapsulin was disassembled with 7 M GuHCl and 100 μg of *sf*GFP-CLP was incorporated with HEPES (50 mM, pH 7.4) buffer during the 1:10 reassembly reaction. For disassembly/reassembly rate measurements, encapsulin was disassembled with either 6 M GuHCl, pH 3, or pH 13 conditions.

Disassembly/Reassembly Characterisation Measurements

Intrinsic tryptophan fluorescence (ITF) measurements of encapsulins in their varying states of assembly were performed with an FP-8500 Spectrofluorometer (JASCO) using a 3 mm pathlength quartz cuvette. 50 μL samples were prepared in triplicate with a final encapsulin concentration of 5 μM. For disassembly/reassembly rate experiments, reactions were prepared in the cuvette with measurements initiated immediately. Samples were excited at 290 nm and emission spectra were collected from 300-550 nm. The typical parameters used were excitation and emission bandwidths of 5 nm, response of 0.2 s, medium sensitivity, data interval of 0.1 nm, scan speed of 100 nm/min, and 4 measurement accumulations were averaged. For time dependent measurements (disassembly/reassembly rate) an emission bandwidth of 2.5 nm, high sensitivity, and 1 measurement accumulation were found to be the optimal parameters. For experiments investigating the effect of temperature, spectra were collected from 20-90°C with a temperature ramp of 2°C/min. The obtained spectra were further processed by buffer spectra subtraction using Spectra Manager™ (JASCO) software, and the ratio between the fluorescence intensity at 330 and 360 nm (330/360) was calculated and plotted in Microsoft Excel.

The secondary structure of encapsulins were analysed via circular dichroism (CD) with a J-1500 CD Spectrometer (Jasco) using a 1 mm pathlength quartz cuvette. To reduce background scattering, encapsulin was buffer exchanged into Milli-Q water using SnakeSkin™ dialysis tubing (10 000 MWCO, 34 mm, ThermoFisher Scientific). Samples of 200 μL were prepared in triplicate as described above, but with a final encapsulin concentration of 0.1 mg/mL and HEPES buffer was substituted with Milli-Q water. Spectra were collected between 180 and 300 nm and CD, HT, and Abs channels were used. A bandwidth of 2 nm, D.I.T of 2 s, data pitch of 0.2 nm, and scanning speed of 100 nm/min were used and 4 accumulations were averaged, except for time dependent measurements where 1 accumulation was taken. Buffer spectra subtraction was applied to obtained spectra using Spectra Manager™ (JASCO) software, and further analysis was done by plotting the signal obtained at 222 nm in Microsoft Excel. Further analysis was done by uploading CD spectra into DichroWeb. Units were converted from mdeg to delta epsilon, reference set 6 optimised for 185-240 nm was selected, and the average was taken from three different analysis programmes (Contin, Selcon3, and CDSSTR).

Dynamic light scattering (DLS) was performed to measure the diameter of encapsulins using a Malvern Zetasizer instrument with a laser wavelength of 633 nm using a 1 cm pathlength polystyrene cuvette. Samples with a final encapsulin concentration of 5 μM were prepared as described above. Three measurements were performed at 25°C, with automatic determination of optimum attenuator condition and measurement position. Data analysis was done with Zetasizer Nanoseries software and distribution analysis data were recorded.

Transmission electron microscopy (TEM) was performed using a Philips CM10 microscope (100 kV accelerating voltage) to visualise morphology, size, and state of encapsulin assembly. Encapsulin samples (0.2 mg/mL) were adsorbed onto pioloform-coated 200 mesh copper grids (ProSciTech) and negatively stained for 1 h using uranyl acetate replacement (UAR) prior to imaging.

2.3 Capture of sfGFP by Encapsulin

The heat stability of GFPnb-ESig and GFPnb-ESig$_T$ was investigated by incubating at 65°C for 15 min followed by centrifugation (13,000 xg, 4°C, 30 min) with the supernatant retained. The binding of *sf*GFP to both nanobodies was facilitated by mixing in a 1:1 ratio and incubating in the dark for 30 min. The binding of heat-treated and non-heated nanobody samples were confirmed and compared by Native-PAGE. Further Native-PAGE gels were used to determine the optimal binding ratios and concentrations of encapsulin and '*sf*GFP + GFPnb-ESig' complex for effective capture. For capture, a 1:3 binding ratio of *sf*GFP (0.3 mg/mL) and GFPnb-ESig (0.9 mg/mL) was mixed and incubated in the dark at room temperature for 30 min. Encapsulin (40 μM) was disassembled as described above with GuHCl (7 M), and reassembled overnight in the presence of the '*sf*GFP + GFPnb-ESig' complex with a final concentration of 0.05 mg/mL. Controls to investigate if the complex was non-specifically bound to the exterior of encapsulin were prepared by mixing 40 μM of self-assembled encapsulin with 0.05 mg/mL of complex. Native-PAGE gels was run at 200 V for 120 min in the dark to preserve fluorescence.

2.4 Capture of α-synuclein by Encapsulin

HiLyte™ Fluor 488 labelled recombinant human α-synuclein (AnaSpec) was mixed with Syn2nb-ESig at a 1:5 ratio (0.2:1 mg/mL, respectively) and incubated in the dark at room temperature for 1 h. Encapsulin (40 μM) was disassembled as described above with GuHCl (7

M), and reassembled overnight in the presence of the 'α-synuclein + Syn2nb-ESig' complex with a final concentration of 0.36 mg/mL. Controls to investigate if the complex was non-specifically binding to the exterior of encapsulin were prepared by mixing 40 μM of self-assembled encapsulin with 0.36 mg/mL of complex. To investigate the removal of non-specifically bound α-synuclein, samples were either incubated with 10 μg of protease Subtilisin A (Sigma-Aldrich) at room temperature for 3 h (300 rpm), or heat treated at 75°C for 15 min followed by centrifugation (10,000 xg, 4°C, 10 min). Native-PAGE to determine optimum binding ratios of the 'α-synuclein + Syn2nb-ESig' complex were run at 200 V for 30 min, and gels for capture in encapsulin were run at 200 V for 2 h, both in the dark.

Enzyme-linked Immunosorbent Assay (ELISA)

The binding of recombinant human α-synuclein protein (without fluorescent labelling) (ab51189, Abcam) to Syn2nb-ESig was done with varying binding ratios and incubated for 1 h at room temperature, and optimal binding ratios were determined by Native-PAGE analysis. An ELISA was performed to monitor changes in α-synuclein concentrations after addition of the capture system. The DuoSet Human α-synuclein (DY1338-05) ELISA kit (R&D Systems) was used as per manufacturer's instructions. In the assay, varying concentrations of encapsulin were used to capture a consistent concentration of α-synuclein. Encapsulins (concentrations of 100, 200, 400, 800, and 1600 μg/mL) were disassembled as described above with GuHCl (6 M). Reassembly was done overnight in the presence of the 'α-synuclein + Syn2nb-ESig' complex with a 1:2 binding ratio (100:200 ng/mL). To assess whether any components of the capture system affects the ELISA, the following control samples were also prepared: α-synuclein (100 ng/mL), Syn2nb-ESig (200 ng/mL), 'α-synuclein + Syn2nb-ESig' complex (100:200 ng/mL), 6 M GuHCl, capture of α-synuclein without Syn2nb-ESig (100 ng/mL), assembled encapsulin (1600 μg/mL), assembled encapsulin (1600 μg/mL) mixed with α-synuclein (100 ng/mL), and assembled encapsulin (1600 μg/mL) mixed with the 'α-synuclein + Syn2nb-ESig' complex (100:200 ng/mL). All samples were diluted 10x before analysis.

Chapter 3: Characterisation of Encapsulin's Disassembly/Reassembly Mechanisms

As outlined in Chapter 1, encapsulins have recently been loaded via an *in vitro* loading process, in which empty encapsulins were disassembled (under denaturing conditions) and subsequently reassembled (upon returning to normal conditions) in the presence of ESig-tagged cargo, resulting in the cargo's selective encapsulation [50]. However, this process remains underutilised and poorly understood. Thus, to effectively control the *in vitro* loading of ESig-tagged proteins inside encapsulin, the biophysical mechanisms and physicochemical factors underlying this disassembly/reassembly process must be accurately characterised. For this purpose, intrinsic tryptophan fluorescence (ITF) and circular dichroism (CD) spectroscopy were used to monitor the structural changes of encapsulin under varying conditions.

CD measures the difference in absorption of left and right-hand circularly polarised light which gives spectral shapes characteristic of different protein secondary structures [52]. For ITF, the fluorescence emission spectra of the aromatic tryptophan (Trp) residues are measured. Trp fluorescence is very environmentally sensitive, thus, indicative of the local chemical environment surrounding the Trp residues [53]. Changes in the exposure of Trp results in a change in the maximum fluorescence emission wavelength, which can be used to monitor protein conformational changes in tertiary structure [53]. ITF and CD are particularly well-suited to the study of dynamic protein structures as they do not require destructive sample preparation and therefore samples can be monitored over time in solution to analyse structural effects of changing conditions [54]. Additionally, these methods are non-invasive and do not require proteins to be labelled which could alter their native shape [53].

Each subunit of encapsulin from *Thermotoga maritima* (TM) contains five Trp residues and is therefore suitable for ITF analysis (Fig. 4a). However, there are no published records of this technique being applied to encapsulins to-date, so initial scans comparing assembled and disassembled encapsulin were done to determine the techniques suitability. Encapsulin was recombinantly expressed in BL21 *Escherichia coli* cells and subsequently purified via size exclusion chromatography (SEC) followed by anion exchange chromatography, confirmed by SDS-PAGE and Native-PAGE analysis (Supp. Fig. S1.a, b, c, d). It should be noted that this is a previously optimised protocol from our lab which has been validated using TEM, DLS, and mass spectrometry. Encapsulin was then disassembled via incubation for 1 h in 7 M guanidine

hydrochloride (GuHCl), as these conditions were previously confirmed to facilitate disassembly [50]. Assembled encapsulin (5 μM) was subject to ITF and displayed a maximum emission wavelength of ~334 nm, whereas disassembled encapsulin (5 μM) demonstrated a red shift to ~355 nm (Fig. 4b). Fully exposed Trp in solvent has a maximum emission of over 350 nm, and therefore 7 M GuHCl appeared to completely disassemble encapsulin [55]. These results showed ITF could discriminate between the maximum emission wavelength of buried Trp in assembled form and solvent exposed Trp in disassembled form in an encapsulin system and was therefore suitable to monitor assembly/disassembly states of encapsulin for subsequent analyses.

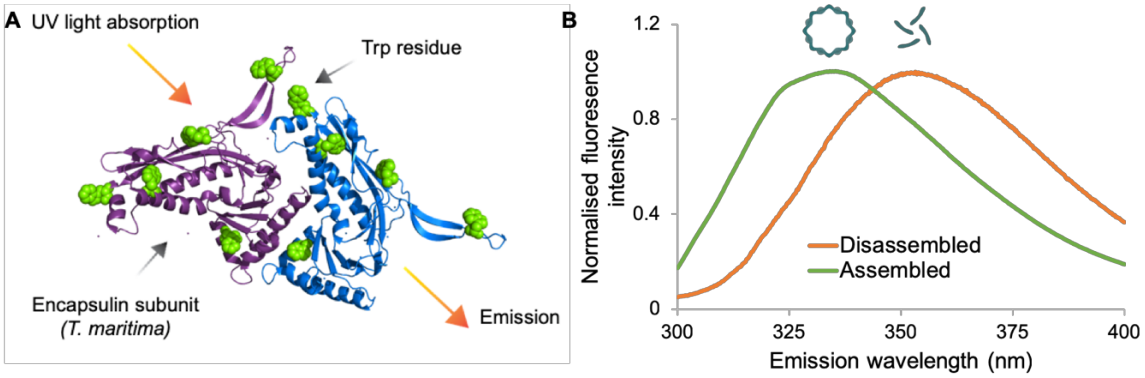

Figure 4: (A) The shift in light emission from Trp residues was used to monitor assembled/disassembled forms of Enc. Enc is made of 60 subunits, each containing five Trp residues (image obtained from PyMOL). **(B)** ITF discriminated between the maximum emission wavelength of buried Trp in assembled form (~334 nm) and solvent exposed Trp in disassembled form (~355 nm).

To assess encapsulins thermostability, assembled encapsulin was heated to 90°C with ITF and CD measurements taken every 10°C. ITF data is presented as a fluorescence intensity ratio of emissions at 360 nm over 330 nm (360/330), as a proxy for the wavelength of maximum fluorescence emission. This ratio is commonly used as an indicator of tertiary structure as it gives information of the degree of protein core solvation [56]. ITF results showed encapsulin remained stable throughout heating with only a very slight observed red shift in emission wavelength at temperatures above 80°C (Fig. 5a). Measurements were done in triplicate with standard error bars calculated but are not visible due to being very small. Encapsulin has a primarily α-helical structure, and the CD spectra of encapsulin (Fig. 5b) displays the maximum mdeg at approximately 195 nm and double minima at approximately 208 and 222 nm

expected for largely α-helical structures [52]. The mdeg at 222 nm was plotted for CD analysis, due to this measurement being a key signature unique to α-helical structure when analysing α-helical proteins. A melt curve was made with the difference of CD mdeg at 222 nm at each temperature compared to the mdeg at 20°C (normalised to 0) and 90°C (normalised to 1). As the temperature of encapsulin increased, the mdeg at 222 nm also increased, indicating a loss of helicity (Fig. 5c). This change in structure was reversible as upon cooling, encapsulin returned to its original structure. The melt curve demonstrated thermal hysteresis, where heating and cooling does not follow a single pathway which is often observed in dynamic proteins (Fig. 5c). CD signal spectra were analysed with DichroWeb and indicated a ~5% loss of helical structure when heated to 90°C, which was recovered when cooled back to 20°C (Fig. 5b). Together, these results support the known thermostability of TM encapsulin, which is derived from the thermophilic bacterium *Thermotoga maritima* [57]. When heated to 90°C the change in structure suggests reversible partial unfolding between subunits, but not complete disassembly. This indicates a very stable tertiary structure of the subunits with a less stable quaternary structure of the cage.

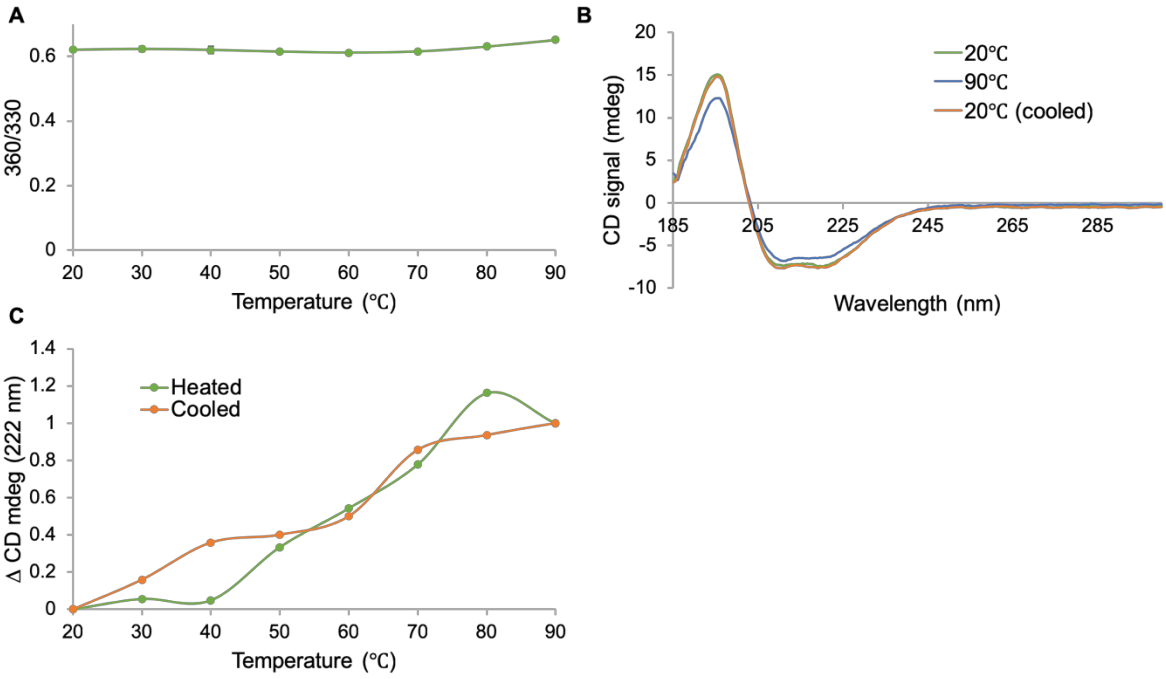

Figure 5: Analysis of Enc whilst heating to 90°C. (A) ITF emission wavelengths (360/330) of Enc between 20-90°C (n = 3). **(B)** Full CD spectra of Enc at 20°C, heated to 90°C, and cooled back to 20°C showing a reversible loss of ~5% helicity that was recovered upon cooling (n = 1). **(C)** The difference in CD mdeg (222 nm) of Enc at each temperature compared to 20°C (normalised to 0) and 90°C (normalised to 1) forming a hysteresis melt curve (n = 1).

Encapsulin was subjected to varying concentrations of GuHCl for 1 h to determine the concentration at which encapsulin disassembly is initiated using ITF. The dotted line represents the maximum emission of assembled encapsulin (360/330), and an observed red shift in emission wavelength indicated disassembly began from approximately 3 M GuHCl (Fig. 6a). For CD analysis, only data below a high-tension voltage (HT) of 600 was plotted, as CD spectra beyond 600 contains excessive noise and is therefore unreliable [52] (Fig. 6b). Therefore, data above 213 nm could not be collected due to the high absorbance of background buffer and further analysis with DichroWeb could not be performed. However, insight into helical changes could still be obtained by monitoring the available CD spectra in the 222 nm region. CD spectra showed a gradual decrease in CD signal intensity in the range of 222 nm, consistent with a loss in helical structure, with spectra at GuHCl 6 M and 7 M having minimal signal at around 222 nm (i.e. <2 mdeg) consistent with a random coil structure, indicating complete disassembly of encapsulin (Fig. 6b). Monitoring the change in CD at 222 nm was consistent with the change in Trp exposure (Fig. 6a, c). To complement

these results, disassembled encapsulin was subject to reassembly in the presence of ESig-tagged superfolder green fluorescent protein (*sf*GFP). Bands present in Coomassie-stained Native-PAGE gel analysis showed all encapsulin samples were intact (either non-disassembled or reassembled) (Fig. 6d). The excitation of fluorescent bands in the same gel between 4–7 M GuHCl confirmed that the encapsulin had disassembled, enabling ESig-tagged *sf*GFP to be *in vitro* loaded into encapsulin during its reassembly (Fig. 6e). In contrast, the absence of fluorescent bands at 0–3 M GuHCl indicated that encapsulin was unable to disassemble at these concentrations, thus preventing the *in vitro* loading of ESig-tagged *sf*GFP (Fig. 6e).

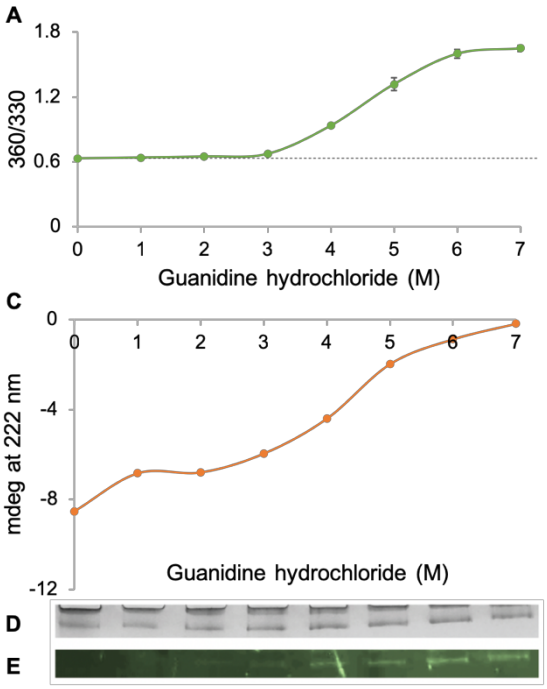

Figure 6: Analysis of Enc after incubation in 0-7 M GuHCl. (A) ITF showed an observed shift in emission wavelength (360/330) and indicated disassembly begins from 3 M (n = 3). Dotted line represents (360/330) of assembled Enc. **(B)** Full CD spectra of Enc showing the gradual decrease in signal intensity in the range of 222 nm (n = 1). **(C)** Decreasing CD mdeg at 222 nm of Enc (n = 1). **(D)** Coomassie stained Native-PAGE showing intact Enc (non-disassembled or reassembled) after incubation in 0-7 M GuHCl (n = 1). **(E)** *sf*GFP fluorescence analysis of the same gel with bands indicating *sf*GFP *in vitro* loading that can only occur during Enc reassembly (i.e. disassembly required).

As 6 M was the lowest GuHCl concentration that displayed complete encapsulin disassembly, this concentration was used for further GuHCl-based experiments. Encapsulin was incubated in 6 M GuHCl over the course of 1 h, with ITF and CD spectra measured at 5 min intervals. The difference in emission compared to assembled encapsulin (normalised to 0 and represented by the red point) was plotted. ITF replicates 1 and 2 show Trp was exposed rapidly and therefore disassembly occurred completely within 5 min of incubation in GuHCl (Fig. 7a). Replicate 3 displayed a more gradual disassembly, however it is possible encapsulin was not mixed sufficiently in the GuHCl (Fig. 7a). The CD spectra also showed a rapid increase of mdeg

at 222 nm within 5 min, indicating a loss of helical structure and disassembly of encapsulin (Fig. 7b).

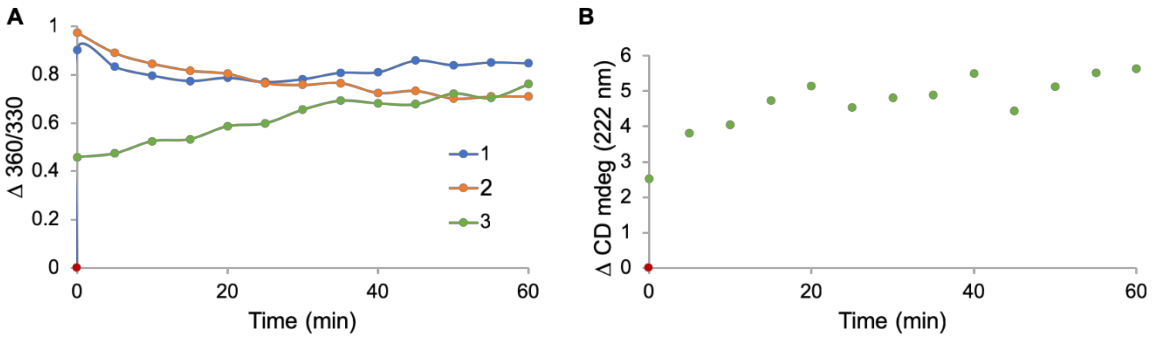

Figure 7: Analysis of Enc in 6 M GuHCl monitored over 1 h. (A) ITF analysis of Enc disassembly by 6 M GuHCl over the course of 1 h. The difference in emission wavelength (360/330) to assembled Enc (normalised to 0 and marked in red) was plotted (n = 3) and showed a rapid red shift of Trp exposure in 5 min. Lines are not fitted and are just to guide the eye. **(B)** CD analysis of Enc disassembly by 6 M GuHCl over the course of 1 h. The difference in CD mdeg at 222 nm to assembled Enc (normalised to 0 and marked in red) was plotted (n = 1) and showed a rapid increase of mdeg at 222 nm within 5 min.

Encapsulin was subject to varying pH conditions for 1 h, with ITF spectra indicating change in Trp exposure occurred only at extreme alkaline conditions at pH 12 and 13 (Fig. 8a). For CD analysis, data beyond 206 nm could not be collected due to high absorbance of background buffer. CD spectra at all pH conditions have minima at approximately 208 and 222 nm consistent with α-helical structure (Fig. 8b). pH 13 CD spectra shows a significant loss of signal around the 222 nm range, consistent with loss of helical structure (Fig. 8b). However, the 208/222 nm minima are still apparent, suggesting at least some of encapsulin's secondary structure remains intact when compared to the complete loss of structure when incubated with high concentrations of GuHCl (Fig. 8b). CD spectra also showed a loss of helical structure at pH 4 and pH 12 (Fig 8.b, c). The samples were incubated in all pH conditions for another 24 h, and pH 12 and pH 13 conditions displayed further loss of helical structure, whereas all other pH conditions remained stable (Supp. Fig. S2.a, b). Encapsulin was incubated in pH 13 for 1 h, with ITF spectra measured at 5 min intervals. The difference in emission compared to assembled encapsulin (made to be 0 and represented by the red point) was plotted. Both replicates show a gradual exposure of Trp that plateaus at ~40 min and indicates encapsulin in pH 13 disassembles at a slower rate and to a lesser degree than in 6 M GuHCl (Fig. 8d). Together, these results suggest that in high GuHCl concentrations encapsulin completely

unfolds and dissociates into its individual subunits, whereas in extreme pH conditions encapsulin maintains some residual structure.

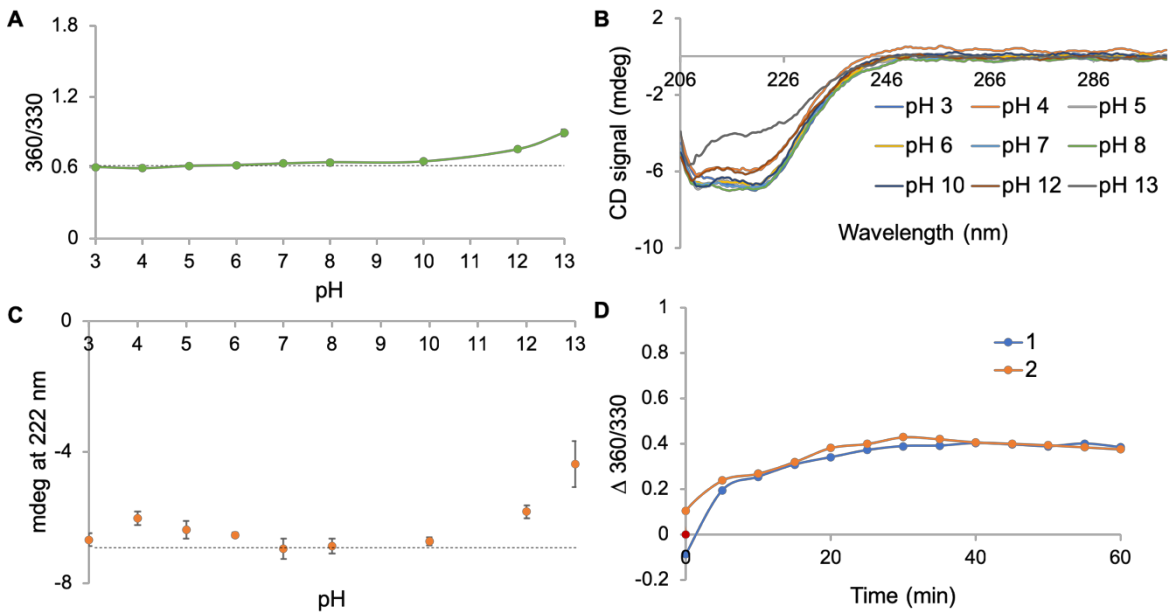

Figure 8: Analysis of Enc after incubation in pH 3-13. (A) An observed shift in ITF emission wavelength (360/330) indicates Trp exposure from pH 12 (n = 3). Dotted line represents (360/330) of assembled Enc. **(B)** Full CD spectra of Enc showed all pH conditions have minima at approximately 208 and 222 nm, with a significant loss of 222 nm signal at pH 13 (n = 1). **(C)** CD mdeg at 222 nm showed an increase at pH 4, 12, and 13 (n = 3). Dotted line represents mdeg (222 nm) of assembled Enc. **(D)** ITF analysis of Enc disassembly by pH 13 over the course of 1 h. The difference in emission wavelength (360/330) to assembled Enc (normalised to 0 and marked in red) was plotted (n = 2) and showed a gradual red shift of Trp exposure that plateaued at ~40 min. Lines are not fitted and are just to guide the eye.

Encapsulin reassembly was measured over 16 h every 30 min after being disassembled with either 6 M GuHCl or pH 13. The difference in emission compared to disassembled encapsulin after being incubated in each condition for 1 h (normalised to 1 and represented by the red point) was plotted. Reassembly after pH 13 disassembly appeared to occur faster with Trp emission plateauing at $t_{1/2} \approx$ 6 h (300 min) compared to disassembly via GuHCl at $t_{1/2} \approx$ 8 h (480 min) (Fig. 9a, b), which may be explained by encapsulin still maintaining some structure after incubation in pH 13 conditions. Reassembly in both conditions appeared to display a two-step reassembly pathway: a quick phase (inset) which may represent the refolding of subunits, and a slow phase possibly representing the reassembly of the cage (Fig. 9a & b). The difference in intensity between replicates suggests each replicate may have differing proportions or extent of assembly but follow the same trend. CD spectra of reassembly after 6 M GuHCl disassembly

demonstrated a more gradual increase of signal, hence helical structure, that plateaued much later at ~8 h (480 min) (Fig. 9c). Together, the ITF results may indicate a rapid burial of Trp residues as individual subunits interact with one another, and the CD results show the more gradual process of the secondary structure interactions required for assembly of the cage. This may suggest the subunits rapidly form stable dimers that then interact with each other gradually to form the cage. This pathway was suggested by Snijder et al. [58] who found encapsulin from *Brevibacterium linens* (also T = 1) displayed a preference for even-numbered stoichiometries via mass spectrometry analysis.

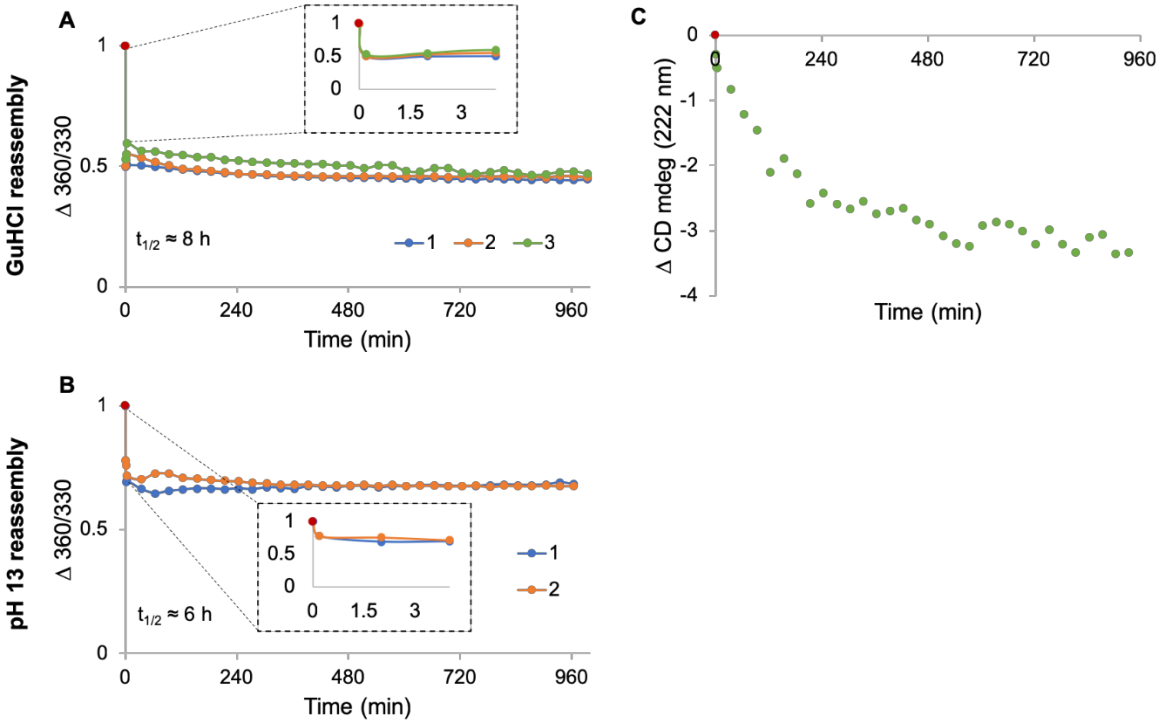

Figure 9: Analysis of Enc reassembly over 16 h after being disassembled by either 6 M GuHCl or pH 13 and being returned to normal conditions. The difference in emission compared to disassembled encapsulin (normalised to 1 and represented by the red point) was plotted. **(A)** ITF showed after GuHCl disassembly Enc reassembled in a two-step pathway, with Trp burial occurring in a quick phase (inset), and a slower phase that plateaued at ~480 min (n = 3). **(B)** ITF showed after pH 13 disassembly Enc reassembled in a two-step pathway, with Trp burial occurring in a quick phase (inset), and a slower phase that plateaued at ~300 min (n = 2). **(C)** CD mdeg at 222 nm of reassembly after GuHCl disassembly showed a more gradual recovery of signal at 222 nm, that plateaued at ~480 min (n = 1).

To complement the above results, disassembly of encapsulin using 6 M GuHCl and subsequent reassembly was also assessed visually using transmission electron microscopy (TEM) and by measuring its diameter using dynamic light scattering (DLS) using the average

of the number means. TEM images of self-assembled encapsulin displayed structures with consistent shape and size and DLS analysis indicated a diameter of 25 ± 1 nm, consistent with its crystal structure data [57] (Fig. 10a). When incubated with 6 M GuHCl for 1 h, no structures were observed in TEM images and DLS showed a diameter of 0.3 ± 0.1 nm, indicating encapsulin had completely disassembled into its subunits (Fig. 10b). Disassembled encapsulin was then returned to normal conditions and allowed to reassemble for 16 h. TEM analysis showed uniform structures similar to that of self-assembled encapsulin, indicating its successful reassembly (Fig. 10c). DLS indicated a ~2 nm increase of diameter of reassembled encapsulin (27.5 ± 2.4 nm) compared to self-assembled encapsulin (Fig. 10c). A slight increase in size of reassembled encapsulin to its native form has also been observed in other encapsulin studies [59]. TEM and DLS analysis of encapsulin disassembled in pH 13 conditions and then reassembled will be done in future studies.

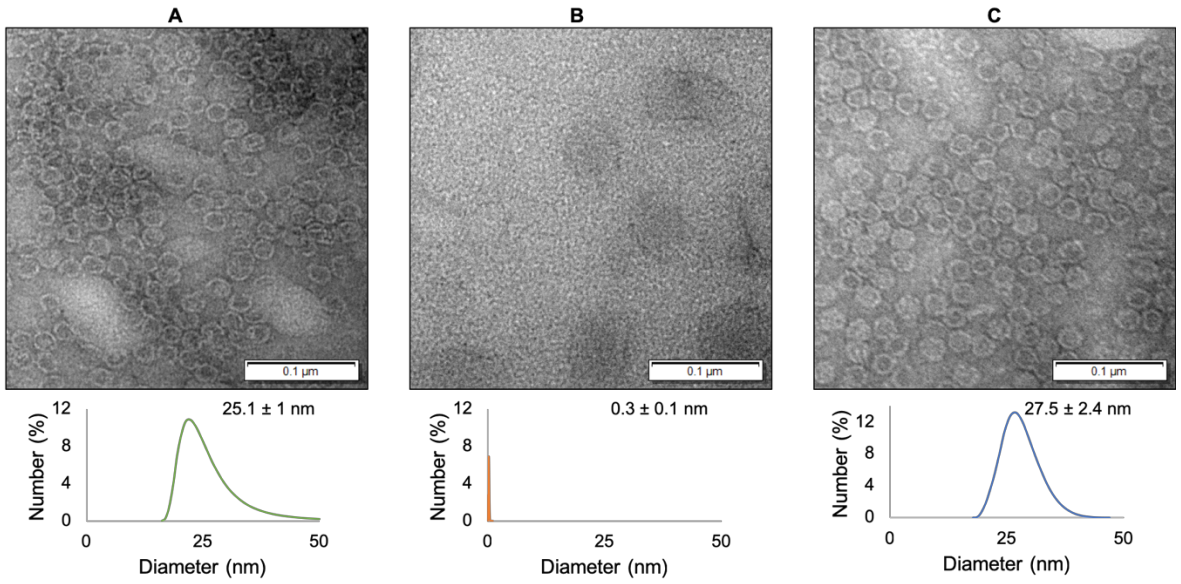

Figure 10: TEM images (magnification 92000x) and DLS results of self-assembled, disassembled, and reassembled Enc. (A) Self-assembled Enc showed a uniform size/shape with a diameter of 25 ± 1 nm. **(B)** Disassembled Enc via 6 M GuHCl showed no structures in TEM images and had a diameter of 0.3 ± 0.1 nm, indicating complete disassembly. **(C)** Reassembled Enc showed the return to a uniform size/shape and a diameter of 27.5 ± 2.4 nm.

To investigate whether size and structure influences disassembly/reassembly, preliminary characterisation experiments were done with larger and more structurally complex encapsulins from *Myxococcus xanthus* (MX) (T = 3 (180 subunits, 32 nm)) and *Quasibacillus thermotolerans* (QT) (T = 4 (240 subunits, 42 nm)) [47-49]. MX and QT encapsulins were

recombinantly expressed in BL21 *E. coli* cells and subsequently purified via SEC followed by anion exchange chromatography, confirmed by TEM analysis (Fig. 11a, b). TEM images of assembled MX showed two differently sized structures, which is consistent with previous studies that show MX can assemble into both a T = 1 and T = 3 structure [49] (Fig. 11a). Comparatively, assembled QT displayed a uniform larger T = 4 size (Fig. 11b). MX and QT were incubated in 6 M GuHCl for 1 h and measured using ITF and DLS to determine if disassembly occurred. ITF fluorescence for both encapsulins demonstrated a red shift in Trp fluorescence after incubation with GuHCl similar to that displayed by TM encapsulin (Fig. 11c, d). DLS analysis of assembled MX showed an average diameter of ~32 nm and QT ~39 nm. After incubation with 6 M GuHCl, DLS analysis of MX and QT showed an average diameter of ~0.12 and ~0.27 nm, respectively. Together, these results show encapsulin from MX and QT completely disassemble in 6 M GuHCl, similar to encapsulin from TM. Future work will investigate the effect pH has on these encapsulins, and their reassembly kinetics will be evaluated.

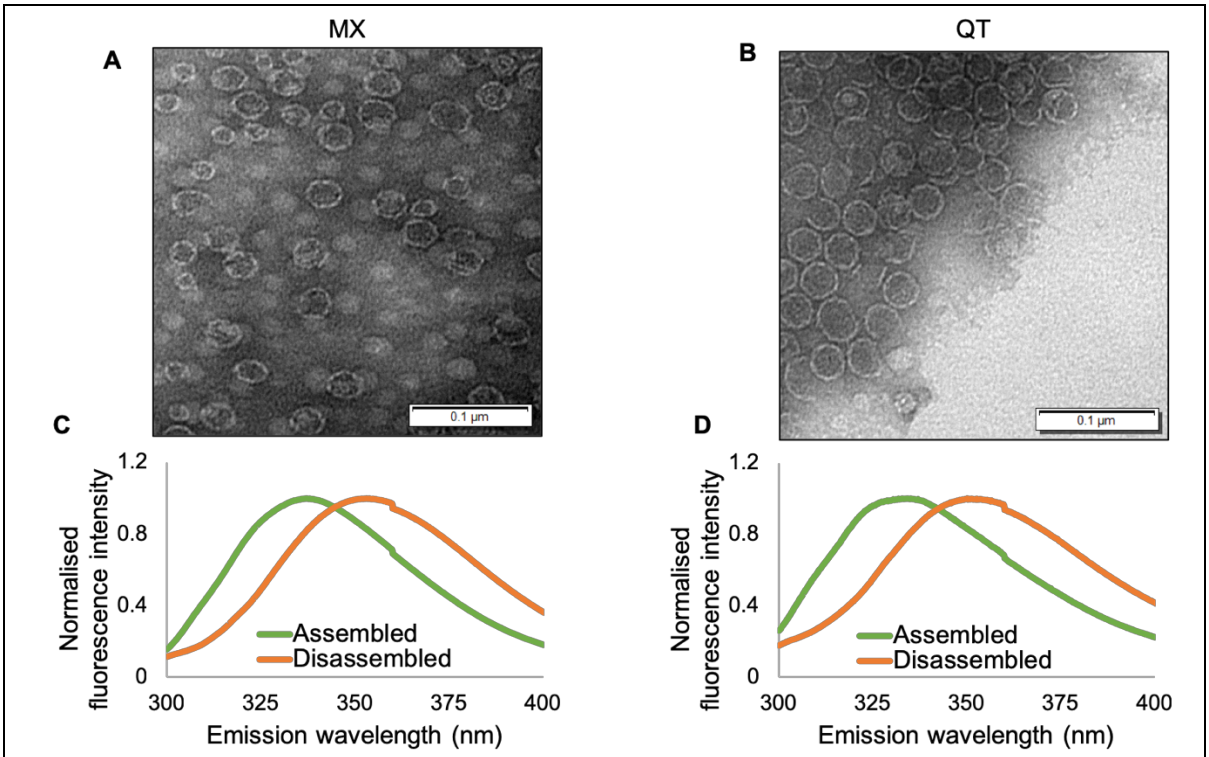

Figure 11: (A) TEM image of self-assembled MX Enc showing the formation of both T = 1 and T = 3 structures. **(B)** TEM image of self-assembled QT Enc showing the formation of uniform T = 4 structures. **(C)** ITF of the maximum emission wavelength of assembled and disassembled MX Enc showing an observed red shift after disassembly in 6 M GuHCl. **(D)** ITF of the maximum emission wavelength of assembled and disassembled QT Enc showing an observed red shift after disassembly in 6 M GuHCl.

The results in this chapter show that encapsulin is a thermostable protein that can be disassembled with high GuHCl concentrations and extreme alkaline conditions to varying degrees and reassembles within 6-8 hours when returned to normal conditions via a two-step kinetic pathway. Furthermore, the ability for ITF to monitor structural changes was successfully evaluated for the first time in an encapsulin system.

The *in vitro* disassembly/reassembly of encapsulins has been seldom explored, and therefore there are multiple avenues for future studies. For example, the effect of disassembly agents other than GuHCl and pH could be evaluated (e.g. oxidation-reduction reactions). The re-formation of capsid shells is highly dependent on subunit concentration and temperature [60]. It is therefore likely that encapsulin is also dependent on these conditions and optimal reassembly concentrations and temperatures could be explored in future studies. Many capsid-like structures have been found to not completely reassemble due to the energetically unfavourable binding process of final subunits, including encapsulin from *B. linens* which was found to often only reassemble with 58 subunits instead of 60 [58].

The spectroscopy techniques used in this chapter are unable to detect if this also happens to encapsulin from TM, and therefore mass spectrometry could be employed in future work.

In the context of applying this system to capture foreign proteins, the effect cargo and complex biological solutions has on the stability and reassembly kinetics will be important to determine. Finding the minimum concentration required for reassembly is also significant in a clinical setting, as this will determine future dosage. This work will provide valuable insights into the cargo-loading properties of encapsulins, furthering their development as drug delivery vehicles.

Chapter 4: Capturing an Unmodified Foreign Protein Using Encapsulins

During their *in vivo* self-assembly, encapsulins recognise and assemble around proteins that display an ESig, packaging them (*in vivo* loading). Alternatively, encapsulins can be purposely dissembled *in vitro* and then reassembled in the presence of ESig-tagged proteins, encapsulating them (*in vitro* loading) [50]. The ability to selectively load ESig-tagged foreign proteins into encapsulin highlights its potential as a nanocarrier system for the delivery of biotherapeutics. However, reprogramming the encapsulin protein loading mechanism to 'capture' unmodified proteins (i.e. no ESig) in biomedical applications remains unexplored. Therefore, in this chapter, I investigate the ability of the encapsulin from *Thermotoga maritima* to specifically capture unmodified *sf*GFP.

As illustrated in Figure 12, the proposed 'capture system' first involves genetically fusing an ESig to an anti-*sf*GFP nanobody. This ESig-tagged nanobody would then bind to *sf*GFP, indirectly attaching an ESig. Finally, the ESig-tagged nanobody + *sf*GFP complex would be mixed with disassembled encapsulin (i.e. encapsulin subunits) and selectively captured during *in vitro* encapsulin reassembly.

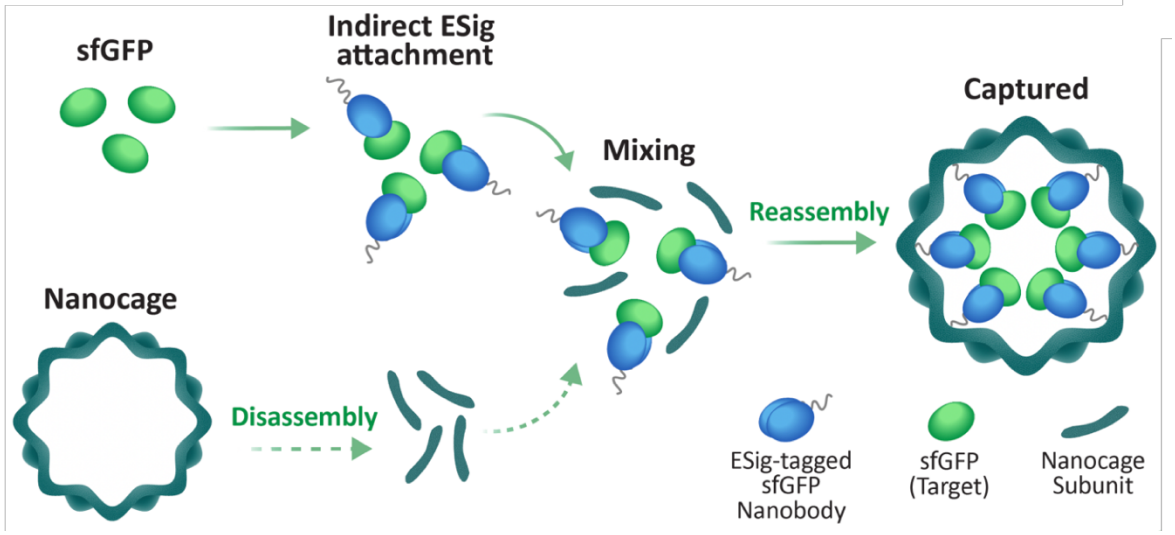

Figure 12: Schematic showing the targeted capture of unmodified sfGFP by Enc. Herein, an ESig-tagged sfGFP nanobody binds to sfGFP (target), indirectly labelling it with an ESig. The resulting 'sfGFP + nanobody' complex is mixed with disassembled Enc and selectively captured during reassembly. Abbreviations: Enc = encapsulin; Esig = encapsulation signal; sfGFP = superfolder green fluorescent protein.

A previously reported nanobody that specifically binds to GFP and its variants (including *sf*GFP) [61] was genetically fused with either (i) a full length ESig (30 aa), (ii) a truncated ESig ('$ESig_T$', 15 aa), or (iii) a full length ESig and His-TEV sequence (for purification purposes). Native-PAGE analysis showed all nanobody variants successfully bound to unmodified *sf*GFP, forming the 'sfGFP + nanobody' complex as indicated by the presence of fluorescent bands with an increased kDa compared to unbound *sf*GFP (Fig. 13). The His-TEV tagged nanobody demonstrated a considerably lower binding affinity compared to non-His-TEV tagged nanobodies, suggesting that the His-TEV sequence may interfere with the *sf*GFP + nanobody complex formation. To determine if the nanobody constructs could be partially purified by a heat treatment step, samples were subjected to 65 °C for 15 min. All heat-treated constructs demonstrated higher purity compared to non-heated samples, showing an observable reduction in background *E. coli* host proteins (Fig. 13). The constructs also displayed good thermostability as they maintained the ability to bind to *sf*GFP after heating (Fig. 13). Collectively, these results demonstrate that an ESig can be indirectly attached to unmodified *sf*GFP (via an ESig-tagged anti-GFP nanobody). Based on these results, we selected the anti-GFP nanobody tagged with a full-length ESig (GFPnb-ESig) for use in subsequent capture experiments.

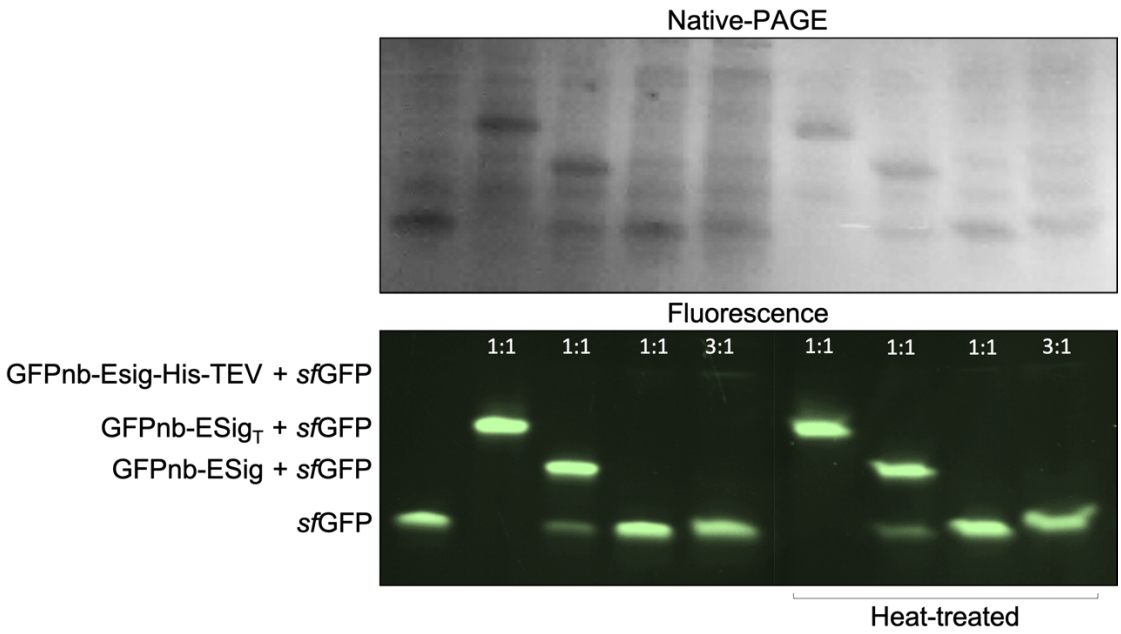

Figure 13: Native-PAGE gel analysis showing the binding of ESig-tagged anti-GFP nanobodies to unmodified sfGFP (i.e. sfGFP + nanobody complex). (Upper panel) Coomassie-stained gel showing the comparison of purity between heated and non-heated nanobodies. **(Lower panel)** the fluorescence of the same gel confirming binding between sfGFP and ESig tagged nanobodies. Ratios represent the respective concentrations of sfGFP:ESig tagged nanobody in the complex.

To determine the optimal encapsulin concentration for the capture of unmodified sfGFP, the 'GFPnb-ESig + *sf*GFP' complex (0.60 mg/mL) was formed and then mixed with varying concentrations of disassembled encapsulin. The modified *sf*GFP-ESig was also loaded *in vitro* as a positive control. A fluorescent image scanner was used to visualise in-gel fluorescence because it has a high sensitivity for *sf*GFP detection and does not induce or detect autofluorescence from encapsulin. As shown in Figure 14, fluorescent bands representing successful *in vitro* loading of the *sf*GFP-ESig positive control were observed, but no fluorescent bands were observed for capture samples (Fig. 14a). The absence of any clear protein bands in the capture lanes after Coomassie staining indicates that encapsulin was unable to fully reassemble into its macrostructure, thereby preventing any capture from occurring. Successful reassembly of the *in vitro* loading controls but absence of capture suggests that the concentration of the 'GFPnb-ESig + *sf*GFP' complex may have been too high, causing interference and preventing the encapsulin subunits from binding to each other. This effect has also been observed in studies of the bacteriophage MS2 capsid, where higher cargo

concentrations kinetically prevented capsid dimers from assembling, resulting in a reduced reassembly yield [62].

In order to investigate whether reducing the complex concentration would allow reassembly of the encapsulin macrostructure, varying concentrations of the 'GFPnb-ESig + *sf*GFP' complex were mixed with a constant concentration of disassembled encapsulin. A concentration of 40 μM for encapsulin was selected for these capture experiments since this was the lowest concentration that displayed a visible protein and fluorescent band in the *in vitro* loading controls (Fig. 14a). Lower concentrations of the 'GFPnb-ESig + *sf*GFP' complex (0.025-0.30 mg/mL) led to increased clarity of protein bands compared to the original concentration (0.60 mg/mL), as well as previously unseen fluorescent capture bands (Fig. 14b). These results confirm that decreasing the complex concentration allowed encapsulin to reassemble, and subsequently capture the 'GFPnb-ESig + *sf*GFP' complex.

Since fluorescence was absent when encapsulin was reassembled with *sf*GFP alone, but present when reassembly occurred in the presence of an 'GFPnb-ESig + *sf*GFP' complex, this demonstrates that specific capture of an unmodified protein was successful. Therefore, these results suggest that *sf*GFP can only be captured when indirectly modified to display an ESig (Fig. 14b). To further verify the complex was captured by encapsulin, as opposed to non-specifically binding to its exterior, capture was repeated along with negative controls of self-assembled (non-disassembled) encapsulin mixed with either *sf*GFP alone, or the 'GFPnb-ESig + *sf*GFP' complex. In contrast to the fluorescent band seen in the capture lane, no fluorescent bands were observed in the negative control lanes (Fig. 14c). These findings indicate that the 'GFPnb-ESig + *sf*GFP' complex did not bind to the exterior of encapsulin and was instead captured inside encapsulin during its *in vitro* reassembly.

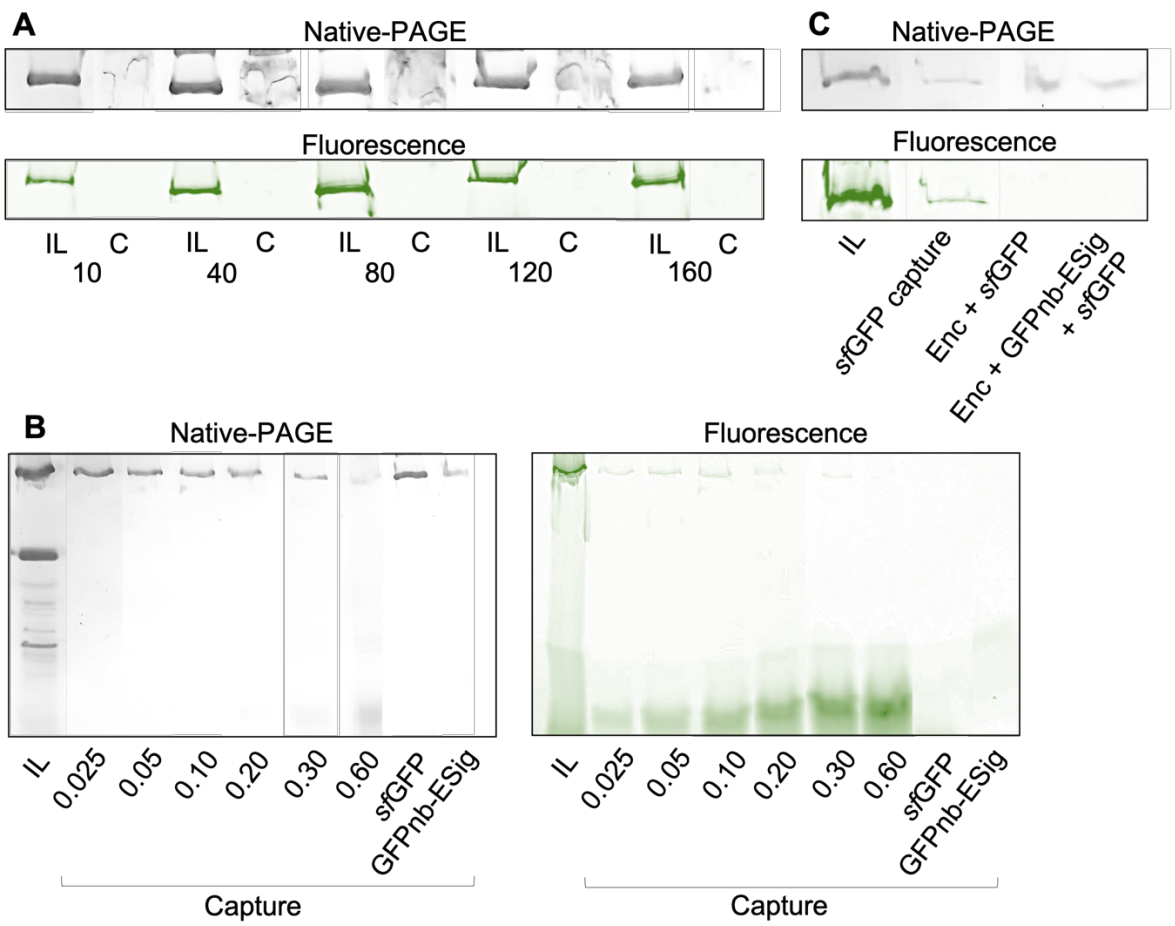

Figure 14: Capture of *sf*GFP. (A) Native-PAGE showing varying concentrations of encapsulin (μM) used for *in vitro* loading (IL) of sfGFP-ESig and the capture of the 'sfGFP + GFPnb-ESig' complex (C). **(Upper panel)** Coomassie stained gel with bands showing encapsulin reassembled during *in vitro* loading, but not during capture. **(Lower panel)** In-gel fluorescence of the same gel demonstrating sfGFP-ESig was loaded into encapsulin during *in vitro* loading, and the absence of bands showing the 'sfGFP + GFPnb-ESig' complex was not captured. **(B)** Native-PAGE of sfGFP capture by encapsulin using varying concentrations of the 'sfGFP + GFPnb-ESig' complex (mg/mL). **(Upper panel)** Coomassie stained gel showing the reassembly efficiency of encapsulin increases as the complex concentration decreases. **(Lower panel)** In-gel fluorescence of the same gel with bands demonstrating capture occurred with complex concentrations 0.025-0.30 mg/mL. The absence of a band for sfGFP alone confirms only specific capture is occurring. **(C)** Native-PAGE showing fluorescence of 'sfGFP + GFPnb-ESig' captured inside Enc. Negative controls of self-assembled Enc mixed with either sfGFP or 'sfGFP + GFPnb-ESig' were performed to confirm that there was no non-specific binding of the target or complex to the outside of Enc, respectively.

Foreign ESig-tagged proteins have been loaded previously *in vitro* during disassembly/reassembly of encapsulin from *T. maritima*. Cassidy et al. [50] used both extreme pH conditions and GuHCl denaturant to disassemble encapsulin, and upon reassembly, successfully loaded *sf*GFP that was genetically modified to contain either a full length or truncated ESig. Similarly, encapsulin was disassembled in extreme acidic conditions (pH 2),

before being brought back to pH 7 in the presence of gold nanoparticles that were functionalised via ligand exchange with a truncated ESig, facilitating their encapsulation [63]. Despite the promise of *in vitro* methods for the loading of ESig-tagged proteins in encapsulin, only the two aforementioned studies have addressed this subject. All other research to date has focused on *in vivo* loading of ESig-tagged proteins through self-assembly of encapsulins inside heterologous hosts. Therefore, progress with *in vitro* methods for encapsulation has been limited.

In vitro disassembly/reassembly mechanisms to load foreign biomolecules have also been applied to other protein-based nanoparticles that share similarities to encapsulins, such as the Cowpea Chlorotic Mottle Virus (CCMV). Minten et al. [64] utilised a heterodimeric coiled-coil protein to function as a noncovalent anchor by genetically fusing a positively charged K-coil to disassembled CCMV subunits, and a negatively charged E-coil to enhanced GFP (EGFP). The modified subunits were kept disassembled at pH 7.5, mixed with EGFP for binding, and subsequently loaded into the capsid as reassembly was initiated at pH 5 [64]. In another study, the bacteriophage MS2 capsid was disassembled into dimers by incubation in glacial acetic acid [62]. Researchers found that encapsulation upon reassembly could be achieved by tagging proteins (GFP and alkaline phosphatase) with either a negatively charged peptide tag via genetic fusion, or by attaching the DNA sequence of the MS2 translational repressor sequence via oxidative coupling [62].

To the best of our knowledge, all previously reported protein-based nanoparticle encapsulation systems rely upon the direct modification of their target protein to facilitate its encapsulation. In contrast, the novel encapsulin-based system outlined in this chapter allows a target protein to be indirectly modified to facilitate its selective capture. This appears to be the first report in which a protein nanoparticle has selectively captured an unmodified protein.

Chapter 5: Capturing α-synuclein Using Encapsulins

The pathological spread of abnormal α-synuclein protein throughout the brain is linked to the progression of Parkinson's Disease (PD) (see Chapter 1 for review). Therefore, the targeted capture and clearance of extracellular α-synuclein may be of great therapeutic benefit, halting or slowing disease progression and reducing intracellular inclusions. Expanding upon the successful proof-of-concept capture of unmodified *sf*GFP (Chapter 4), this chapter explores the potential application of the encapsulin system to capture α-synuclein.

Similar to the *sf*GFP capture system, an ESig would be genetically fused to an anti-α-synuclein nanobody and mixed with α-synuclein to form an 'α-synuclein + ESig-tagged nanobody' complex, indirectly attaching the ESig to α-synuclein (Fig. 15). The complex would then be mixed with disassembled encapsulin and α-synuclein subsequently captured upon reassembly *in vitro*.

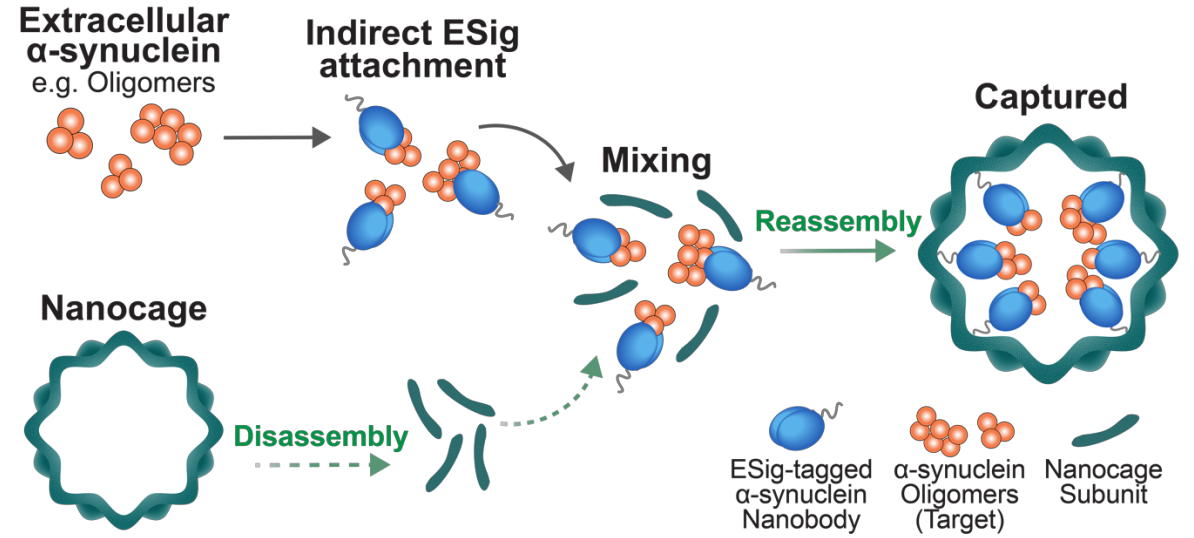

Figure 15: Schematic showing the targeted capture of α-synuclein using Enc. An ESig-tagged anti-α-synuclein nanobody binds to α-synuclein, indirectly labelling it with an ESig. The resulting 'α-synuclein + nanobody' complex is mixed with disassembled Enc and selectively captured during reassembly. Abbreviations: Enc = encapsulin; ESig = encapsulation signal.

A full length ESig (30 aa) was genetically fused to the Syn2 nanobody (Syn2nb-ESig) which has been reported to bind to both monomeric and fibrillar forms of α-synuclein [65]. His-tagged Syn2nb-ESig was recombinantly expressed in BL21 *Escherichia coli* cells and subsequently purified via immobilized metal affinity chromatography (IMAC). Syn2nb-ESig (~18 kDa)

production and purification was confirmed by SDS-PAGE analysis (Supp. Fig. S3). Recombinant human α-synuclein labelled with the fluorescent dye HiLyte™ Fluor 488 (AnaSpec, USA) was mixed with varying concentrations of Syn2nb-ESig. Native-PAGE analysis showed the presence of fluorescent bands with a molecular weight higher than α-synuclein alone, indicating successful formation of the 'α-synuclein + Syn2nb-ESig' complex, and therefore, indirect attachment of an ESig to α-synuclein (Fig. 16a). A 1:1 ratio of α-synuclein to Syn2nb-ESig was not sufficient for binding and was only achieved with a higher ratio of 1:10, suggesting that the fluorescent dye tag on α-synuclein may have inhibited nanobody binding (Fig. 16a).

Varying concentrations of the 'α-synuclein + Syn2nb-ESig' complex were mixed with 40 μM of disassembled encapsulin (previously optimised in Chapter 5), and the observed presence of fluorescent bands during Native-PAGE analysis suggested capture may have occurred (Fig. 16b). However, some fluorescent smearing was also observed for the control samples containing 'assembled' encapsulin mixed with α-synuclein alone or with the complex, suggesting that α-synuclein non-specifically binds to the outside of encapsulin (Fig. 16b). This unwanted binding is likely mediated by the dye conjugated to α-synuclein, as fluorescent probes have been known to non-specifically adsorb to proteins [66]. To accurately determine if any of the complex was captured, we attempted to remove exterior-bound α-synuclein. Herein, capture samples and control samples containing 'assembled' encapsulin mixed with the complex, were exposed to 75°C for 15 min or the protease Subtilisin A for 3 h. In both the non-treated and heat-treated capture samples, a clear fluorescent band was observed, while fluorescent smearing was seen in the assembled controls (Fig. 16c). Subtilisin A appeared to degrade both the capture and assembled control (Fig. 16c). The stronger fluorescent bands of the non-treated and heat-treated capture samples in comparison to the smearing of assembled controls suggests the complex was captured. But as some fluorescence was still observed in the assembled controls, we decided to use non-labelled α-synuclein to help verify capture instead.

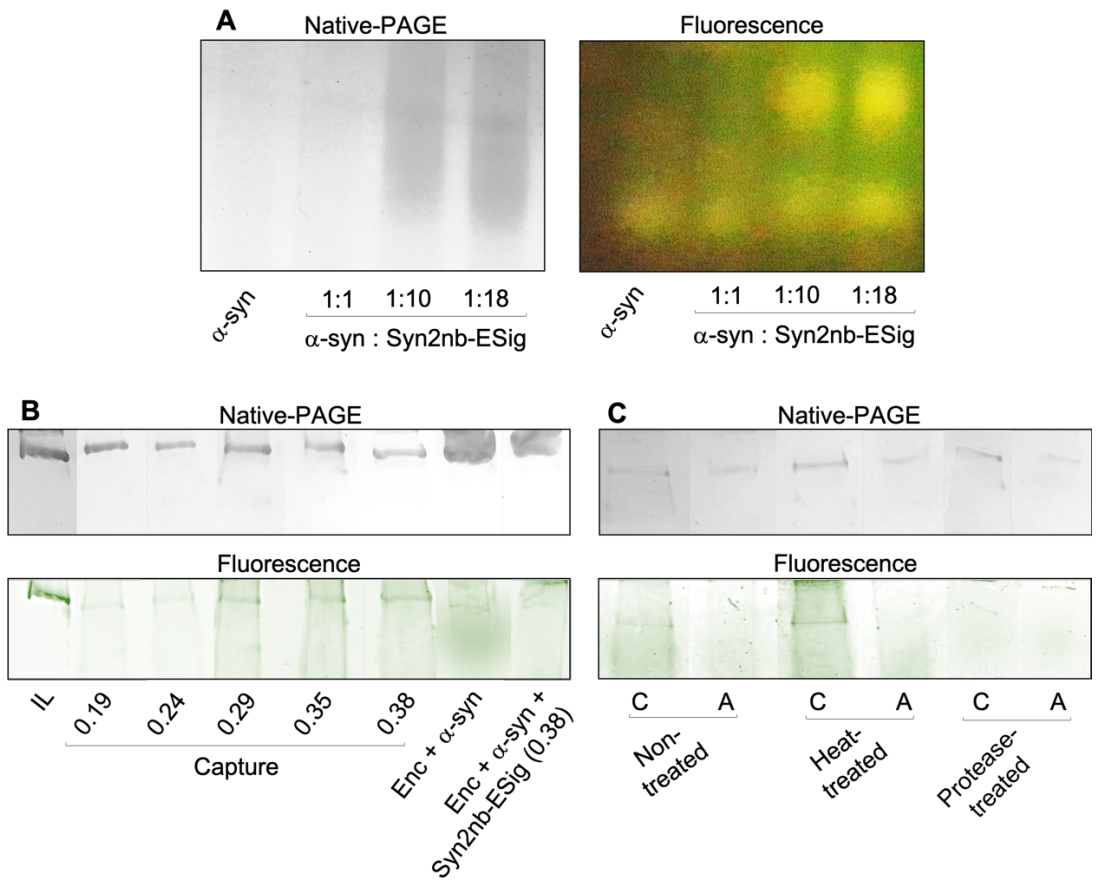

Figure 16: Capture of α-synuclein. (A) Native-PAGE gel analysis showing the binding of ESig tagged nanobodies to α-synuclein (i.e. α-synuclein + nanobody complex). **(Left panel)** Coomassie-stained gel of α-synuclein + nanobody complex. **(Right panel)** Fluorescence of the same gel confirming binding between α-synuclein and ESig-tagged nanobodies. **(B)** Native-PAGE of sfGFP-ESig *in vitro* loading positive control (IL); capture of varying 'α-synuclein + nanobody' complex concentrations; negative controls of assembled Enc mixed with α-synuclein; and assembled Enc mixed with 'α-synuclein + nanobody' complex **(Upper panel)** Coomassie stained gel with bands showing encapsulin reassembled during *in vitro* loading and capture. **(Lower panel)** Fluorescence of the same gel with bands demonstrating 'α-synuclein + nanobody complex' has either been captured or non-specifically bound to the exterior of Enc. **(C)** Native-PAGE of capture samples (C) where Enc was disassembled and reassembled with the complex, and assembled (A) samples where Enc was not disassembled and mixed with the complex. **(Upper panel)** Coomassie stained gel with bands showing encapsulin reassembled. **(Lower panel)** fluorescence of the same gel with bands demonstrating the complex has either been captured or non-specifically bound to the exterior of Enc.

Non-labelled recombinant α-synuclein (ab51189, Abcam) was mixed with varying concentrations of Syn2nb-ESig. A change in molecular weight, when compared to α-synuclein and Syn2nb-ESig alone, indicated the successful formation of the 'α-synuclein + Syn2nb-ESig' complex (Fig. 17). The high mass of Syn2nb-Esig alone is likely due to its structure, which changes upon binding to α-synuclein. We also observed a small excess of unbound α-

synuclein in the native gel, indicating insufficient amounts of Syn2nb-ESig. We therefore applied a 1:2 (α-synuclein:Syn2nb-ESig) ratio in further experiments below.

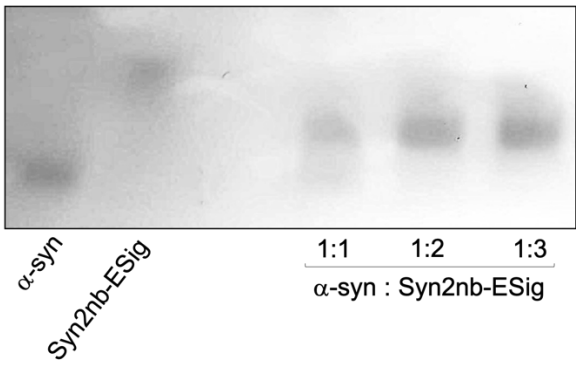

Figure 17: Coomassie stained Native-PAGE showing the formation of the 'α-syn (non-labelled) + Syn2nb-ESig' complex' as indicated by a shift in mass.

The use of non-labelled α-synuclein meant that its capture could not be monitored via fluorescence detection (as attempted above). Therefore, to verify α-synuclein capture and quantify the amount of α-synuclein captured from fluid, we performed an α-synuclein enzyme-linked immunosorbent assay (ELISA). Herein, a consistent quantity of α-synuclein and the 'α-synuclein + Syn2nb-ESig' complex was captured using varying concentrations of encapsulin. The standard curve of α-synuclein indicated that the ELISA itself worked, however, the experimental samples were unfortunately diluted below the detection limit of the assay and were therefore unmeasurable (data not shown). Future ELISA experiments will be carried out with optimal α-synuclein + Syn2nb-ESig complex concentrations, therefore allowing us to verify and quantitatively measure the capture of α-synuclein by the encapsulin system.

The results detailed in this chapter show the successful engineering and production of an ESig-tagged nanobody that can selectively bind to α-synuclein. The *in vitro* capture of α-synuclein in encapsulin may have been observed, but the data currently remains somewhat inconclusive due to the possibility of non-specific binding of the α-synuclein + Syn2nb-ESig to the exterior of encapsulin. Future studies, including ELISA analysis, will be conducted to verify and then optimise the capture of α-synuclein in encapsulin. Another way to verify the capture of α-synuclein could be to determine if externally bound α-synuclein alters the charge of

encapsulin as opposed to α-synuclein being captured inside. If so, anion exchange chromatography could be employed to differentiate between capture and non-specific binding of α-synuclein. Alternatively, α-synuclein could be genetically conjugated with *sf*GFP, thereby allowing the previously used fluorescence detection methods in Chapter 4 to visualise its capture.

Chapter 6: Conclusions and Future Directions

In this study, we employed various spectroscopic and microscopic techniques to investigate the self-assembling properties of encapsulin protein nanocages. Intrinsic tryptophan fluorescence (ITF) spectroscopy revealed itself as a new and accurate method to monitor encapsulin disassembly/reassembly under a range of conditions i.e. exposure to extreme pH, temperature, and denaturant concentrations. We were able to apply our new understanding of encapsulin self-assembly to re-programme the cargo-loading mechanisms of the encapsulin from *T. maritima* to capture unmodified foreign proteins. Herein, the unmodified protein *sf*GFP was successfully captured, and thus, a novel 'capture system' was developed. To the best of our knowledge, this is the first report in which a protein-based nanoparticle has selectively captured an unmodified protein. Finally, to assess its potential future application as a PD therapeutic, our system was customised to capture α-synuclein. Whilst our preliminary data indicated that the system may have captured α-synuclein, these results were ultimately inconclusive. Therefore, experiments will be designed and conducted to verify and then optimise the system for α-synuclein capture. These include ELISA analysis, anion exchange chromatography, and conjugating *sf*GFP to α-synuclein to visually monitor its capture using fluorescent techniques.

Due to the novelty of this first-of-its-kind system, multiple avenues for future optimisation exist. For example, we attempted capture using nanobodies tagged with a full-length ESig (30 aa), while preliminary results indicated that an anti-GFP nanobody with a truncated $ESig_T$ (15 aa) also bound *sf*GFP. Therefore, the effect shorter ESigs have on capture will be assessed as they may allow more cargo to be captured by reducing steric hindrance. Additionally, our preliminary characterisation of the two larger encapsulin systems from MX and QT provide an opportunity to capture α-synuclein more efficiently, thus adapting these systems for capture is an option. Additionally, the α-synuclein used in this work had a monomeric form. As the pathogenicity of α-synuclein in PD is linked to its oligomeric form, future work will investigate the binding and capture of oligomeric α-synuclein for a more representative *in vitro* model.

To understand the potential of the capture system as a treatment strategy for PD, its efficacy and safety in a biological system must first be assessed. This will involve studying the effect encapsulins have on neurons *in vitro* e.g. cell viability, cytotoxicity and oxidative stress.

In this work, encapsulins were recombinantly produced in the bacterium *E. coli*, and are therefore susceptible to endotoxin contamination which may induce adverse pro-inflammatory effects. Consequently, to eliminate unwanted endotoxin contamination, encapsulins can be produced other hosts, such as mammalian cells (e.g. HEK293T cells) or yeast (e.g. *Saccharomyces cerevisiae*) hosts [45, 67]. A co-culture model of α-synuclein transmission comprising a cell-line that overexpresses α-synuclein and a cell-line that is healthy, will be used to assess whether the capture system can reduce extracellular α-synuclein levels and prevent transmission *in vitro* [68, 69]. Upon the establishment of an *in vitro* model of α-synuclein capture, we can begin to investigate whether the capture system can improve disease phenotype in a pre-clinical *in vivo* model of PD [70].

The components of the encapsulin capture system can be easily modified through genetic engineering and therefore beneficial functions can be applied to improve its efficacy. For example, additional ESig-tagged nanobodies that bind to alternative oligomeric forms of α-synuclein could be employed to increase α-synuclein capture. Similarly, the interfaces between subunits could be modified to slow reassembly rates and prolong the body circulation time of disassembled subunits, thereby enhancing encapsulins bioavailability as a therapeutic to capture α-synuclein. The exterior of encapsulin is also available for modification and could be functionalised to display microglia-attracting moieties to facilitate phagocytosis and selective degradation of encapsulin and α-synuclein upon its capture, subsequently clearing it from the extracellular space. In addition, these components are modular and interchangeable, allowing the capture system to be adapted and applied to other neurodegenerative diseases that progress via the extracellular transmission of pathological proteins e.g. hyperphosphorylated tau in Alzheimer's Disease.

Finally, current PD therapeutics only alleviate the symptoms of PD and do not alter the underlying mechanisms that cause its spread throughout the brain. Therefore, a disease modifying treatment for PD remains a significant unmet need. By turning the focus towards therapeutics that target α-synuclein, the pathological spread of PD throughout the brain could be halted. The α-synuclein capture system described in this thesis is unique from other approaches as it is designed to specifically target and remove α-synuclein from the extracellular space. This may prevent its transmission to healthy cells and halt the subsequent misfolding of endogenous α-synuclein within these recipient neurons, which is a newly

identified mechanism of α-synuclein spread, and thereby represents a possible effective treatment for both motor and cognitive impairment in PD.

References

1. Chen, W.W., X. Zhang, and W.J. Huang, *Role of neuroinflammation in neurodegenerative diseases.* J Molecular medicine reports, 2016. **13**(4): p. 3391-3396.
2. Cacabelos, R., *Parkinson's disease: from pathogenesis to pharmacogenomics.* International journal of molecular sciences, 2017. **18**(3): p. 551.
3. Poewe, W., et al., *Parkinson disease.* J Nature reviews Disease primers, 2017. **3**: p. 17013.
4. Billings, J.L., et al., *L-DOPA modulates brain iron, dopaminergic neurodegeneration and motor dysfunction in iron overload and mutant alpha-synuclein mouse models of Parkinson's disease.* Journal of neurochemistry, 2019.
5. Juárez Olguín, H., et al., *The role of dopamine and its dysfunction as a consequence of oxidative stress.* Oxidative medicine and cellular longevity, 2016. **2016**.
6. Braak, H., et al., *Staging of brain pathology related to sporadic Parkinson's disease.* Neurobiology of aging, 2003. **24**(2): p. 197-211.
7. Volpicelli-Daley, L.A., K.C. Luk, and V.M. Lee, *Addition of exogenous α-synuclein preformed fibrils to primary neuronal cultures to seed recruitment of endogenous α-synuclein to Lewy body and Lewy neurite–like aggregates.* Nature protocols, 2014. **9**(9): p. 2135.
8. Lane, E., *L-DOPA for Parkinson's disease—a bittersweet pill.* The European journal of neuroscience, 2018. **49**(3): p. 384-398.
9. YY Szeto, J. and S.J.C.n. JG Lewis, *Current treatment options for Alzheimer's disease and Parkinson's disease dementia.* 2016. **14**(4): p. 326-338.
10. Elkouzi, A., et al., *Emerging therapies in Parkinson disease—repurposed drugs and new approaches.* Nature Reviews Neurology, 2019. **15**(4): p. 204-223.
11. Di Martino, P., et al., *Nano-medicine improving the bioavailability of small molecules for the prevention of neurodegenerative diseases.* 2017. **23**(13): p. 1897-1908.
12. Sharma, G., et al., *Advances in nanocarriers enabled brain targeted drug delivery across blood brain barrier.* 2019.
13. Saraiva, C., et al., *Nanoparticle-mediated brain drug delivery: overcoming blood–brain barrier to treat neurodegenerative diseases.* 2016. **235**: p. 34-47.
14. da Rocha Lindner, G., et al., *Improved neuroprotective effects of resveratrol-loaded polysorbate 80-coated poly (lactide) nanoparticles in MPTP-induced Parkinsonism.* 2015. **10**(7): p. 1127-1138.
15. Molino, N.M. and S.-W. Wang, *Caged protein nanoparticles for drug delivery.* Curr Opin Biotechnol, 2014. **28**: p. 75-82.
16. Pelaz, B., et al., *Surface functionalization of nanoparticles with polyethylene glycol: effects on protein adsorption and cellular uptake.* 2015. **9**(7): p. 6996-7008.
17. Zheng, M., et al., *Nanotechnology-Based Strategies for siRNA Brain Delivery for Disease Therapy.* Trends Biotechnol, 2018. **36**(5): p. 562-575.
18. Hawthorne, G.H., et al., *Nanomedicine to Overcome Current Parkinson's Treatment Liabilities: A Systematic Review.* Neurotox Res, 2016. **30**(4): p. 715-729.
19. Tan, J., et al., *Incorporation of Levodopa into Biopolymer Coatings Based on Carboxylated Carbon Nanotubes for pH-Dependent Sustained Release Drug Delivery* . 2018.

20. McDonagh, B.H., et al., *L-DOPA-Coated Manganese Oxide Nanoparticles as Dual MRI Contrast Agents and Drug-Delivery Vehicles.* Small, 2016. **12**(3): p. 301-306.
21. Kura, A.U., et al., *Acute oral toxicity and biodistribution study of zinc-aluminium-levodopa nanocomposite.* Nanoscale Res. Lett., 2015. **10**(1): p. 1-11.
22. Gonzalez-Carter, D.A., et al., *L-dopa functionalized, multi-branched gold nanoparticles as brain-targeted nano-vehicles.* 2019. **15**(1): p. 1-11.
23. Burkhard, P., et al., *Structural insight into Parkinson's disease treatment from drug-inhibited DOPA decarboxylase.* 2001. **8**(11): p. 963.
24. Sintov, A.C., H.V. Levy, and I.J.P.r. Greenberg, *Continuous transdermal delivery of L-DOPA based on a self-assembling nanomicellar system.* 2017. **34**(7): p. 1459-1468.
25. Sharma, S., et al., *Formulation and characterization of intranasal mucoadhesive nanoparticulates and thermo-reversible gel of levodopa for brain delivery.* 2014. **40**(7): p. 869-878.
26. Borovac, J.A.J.T.Y.j.o.b. and medicine, *Focus: The Aging Brain: Side effects of a dopamine agonist therapy for Parkinson's disease: a mini-review of clinical pharmacology.* 2016. **89**(1): p. 37.
27. Ray, S., et al., *Polysorbate 80 coated crosslinked chitosan nanoparticles of ropinirole hydrochloride for brain targeting.* J. Drug Delivery Sci. Technol., 2018. **48**: p. 21-29.
28. Barcia, E., et al., *Nanotechnology-based drug delivery of ropinirole for Parkinson's disease.* Drug Deliv, 2017. **24**(1): p. 1112-1123.
29. Latt, M.D., et al., *Factors to Consider in the Selection of Dopamine Agonists for Older Persons with Parkinson's Disease.* 2019: p. 1-14.
30. Bi, C., et al., *Intranasal delivery of rotigotine to the brain with lactoferrin-modified PEG-PLGA nanoparticles for Parkinson's disease treatment.* Int. J. Nanomed., 2016. **11**: p. 6547-6559.
31. Yan, X., et al., *Lactoferrin-modified rotigotine nanoparticles for enhanced nose-to-brain delivery: LESA-MS/MS-based drug biodistribution, pharmacodynamics, and neuroprotective effects.* Int J Nanomedicine, 2018. **13**: p. 273-281.
32. Dézsi, L., L.J.C. Vécsei, and N.D.-D. Targets, *Monoamine oxidase B inhibitors in Parkinson's disease.* 2017. **16**(4): p. 425-439.
33. Ahmad, N., *Rasagiline-encapsulated chitosan-coated PLGA nanoparticles targeted to the brain in the treatment of parkinson's disease.* J. Liq. Chromatogr. Relat. Technol., 2017. **40**(13): p. 677-690.
34. Fernandes, C., et al., *PEGylated PLGA nanoparticles as a smart carrier to increase the cellular uptake of a coumarin-based monoamine oxidase B inhibitor.* 2018. **10**(46): p. 39557-39569.
35. Yoosefian, M., et al., *Nanocarrier for levodopa Parkinson therapeutic drug; comprehensive benserazide analysis.* 2018: p. 1-13.
36. Chan, D.K.Y., et al., *Mini-review on initiatives to interfere with the propagation and clearance of alpha-synuclein in Parkinson's disease.* Translational neurodegeneration, 2017. **6**(1): p. 33.
37. Helmschrodt, C., et al., *Polyethylenimine nanoparticle-mediated siRNA delivery to reduce α-Synuclein expression in a model of Parkinson's disease.* Molecular Therapy-Nucleic Acids, 2017. **9**: p. 57-68.
38. Niu, S., et al., *Inhibition by multifunctional magnetic nanoparticles loaded with alpha-synuclein RNAi plasmid in a Parkinson's disease model.* Theranostics, 2017. **7**(2): p. 344.

39. Spencer, B., et al., *Lentivirus mediated delivery of neurosin promotes clearance of wild-type α-synuclein and reduces the pathology in an α-synuclein model of LBD.* Molecular Therapy, 2013. **21**(1): p. 31-41.
40. Taebnia, N., et al., *Curcumin-loaded amine-functionalized mesoporous silica nanoparticles inhibit α-synuclein fibrillation and reduce its cytotoxicity-associated effects.* Langmuir, 2016. **32**(50): p. 13394-13402.
41. Yang, J.A., et al., *Study of wild-type α-synuclein binding and orientation on gold nanoparticles.* Langmuir, 2013. **29**(14): p. 4603-4615.
42. Bobo, D., et al., *Nanoparticle-based medicines: a review of FDA-approved materials and clinical trials to date.* 2016. **33**(10): p. 2373-2387.
43. van der Munnik, N.P., M.A. Moss, and M.J.J.P.b. Uline, *Obstacles to translating the promise of nanoparticles into viable amyloid disease therapeutics.* 2019.
44. Diaz, D., A. Care, and A.J.G. Sunna, *Bioengineering Strategies for Protein-Based Nanoparticles.* 2018. **9**(7): p. 370.
45. Sigmund, F., et al., *Bacterial encapsulins as orthogonal compartments for mammalian cell engineering.* 2018. **9**.
46. Kumari, S., et al., *Overcoming blood brain barrier with a dual purpose Temozolomide loaded Lactoferrin nanoparticles for combating glioma (SERP-17-12433).* Scientific reports, 2017. **7**(1): p. 1-13.
47. Giessen, T.W., et al., *Large protein organelles form a new iron sequestration system with high storage capacity.* Elife, 2019. **8**.
48. Giessen, T.W. and P.A. Silver, *Widespread distribution of encapsulin nanocompartments reveals functional diversity.* Nature microbiology, 2017. **2**(6): p. 17029.
49. Sigmund, F., et al., *Iron-sequestering nanocompartments as multiplexed Electron Microscopy gene reporters.* bioRxiv, 2019: p. 516955.
50. Cassidy-Amstutz, C., et al., *Identification of a minimal peptide tag for in vivo and in vitro loading of encapsulin.* Biochemistry, 2016. **55**(24): p. 3461-3468.
51. Broisat, A., et al., *Nanobodies targeting mouse/human VCAM1 for the nuclear imaging of atherosclerotic lesions.* Circulation research, 2012. **110**(7): p. 927-937.
52. Kelly, S.M., T.J. Jess, and N.C. Price, *How to study proteins by circular dichroism.* Biochimica et Biophysica Acta (BBA)-Proteins and Proteomics, 2005. **1751**(2): p. 119-139.
53. Ghisaidoobe, A.B. and S.J. Chung, *Intrinsic tryptophan fluorescence in the detection and analysis of proteins: a focus on Förster resonance energy transfer techniques.* International journal of molecular sciences, 2014. **15**(12): p. 22518-22538.
54. Henzler-Wildman, K. and D. Kern, *Dynamic personalities of proteins.* Nature, 2007. **450**(7172): p. 964.
55. Bhattacharjee, C. and K. Das, *Thermal unfolding and refolding of β-lactoglobulin: An intrinsic and extrinsic fluorescence study.* European Journal of Biochemistry, 2000. **267**(13): p. 3957-3964.
56. Chaudhary, A.P., et al., *A comparative study of fibrillation kinetics of two homologous proteins under identical solution condition.* Biochimie, 2017. **132**: p. 75-84.
57. Sutter, M., et al., *Structural basis of enzyme encapsulation into a bacterial nanocompartment.* Nature structural and molecular biology, 2008. **15**(9): p. 939.

58. Snijder, J., et al., *Assembly and mechanical properties of the cargo-free and cargo-loaded bacterial nanocompartment encapsulin.* Biomacromolecules, 2016. **17**(8): p. 2522-2529.
59. Rahmanpour, R. and T.D. Bugg, *Assembly in vitro of Rhodococcus jostii RHA 1 encapsulin and peroxidase DypB to form a nanocompartment.* The FEBS journal, 2013. **280**(9): p. 2097-2104.
60. Nguyen, H.D., V.S. Reddy, and C.L. Brooks, *Deciphering the kinetic mechanism of spontaneous self-assembly of icosahedral capsids.* Nano Letters, 2007. **7**(2): p. 338-344.
61. Kubala, M.H., et al., *Structural and thermodynamic analysis of the GFP: GFP-nanobody complex.* 2010. **19**(12): p. 2389-2401.
62. Glasgow, J.E., et al., *Osmolyte-mediated encapsulation of proteins inside MS2 viral capsids.* ACS nano, 2012. **6**(10): p. 8658-8664.
63. Künzle, M., et al., *Peptide-directed encapsulation of inorganic nanoparticles into protein containers.* Nanoscale, 2018. **10**(48): p. 22917-22926.
64. Minten, I.J., et al., *Controlled encapsulation of multiple proteins in virus capsids.* Journal of the American Chemical Society, 2009. **131**(49): p. 17771-17773.
65. Guilliams, T., et al., *Nanobodies raised against monomeric α-synuclein distinguish between fibrils at different maturation stages.* Journal of molecular biology, 2013. **425**(14): p. 2397-2411.
66. Zanetti-Domingues, L.C., et al., *Hydrophobic fluorescent probes introduce artifacts into single molecule tracking experiments due to non-specific binding.* PloS one, 2013. **8**(9): p. e74200.
67. Lau, Y.H., et al., *Prokaryotic nanocompartments form synthetic organelles in a eukaryote.* Nature communications, 2018. **9**(1): p. 1311.
68. Choi, Y.R., et al., *Prion-like Propagation of α-Synuclein Is Regulated by the FcγRIIB-SHP-1/2 Signaling Pathway in Neurons.* 2018. **22**(1): p. 136-148.
69. Reyes, J.F., et al., *A cell culture model for monitoring α-synuclein cell-to-cell transfer.* Neurobiology of disease, 2015. **77**: p. 266-275.
70. Polinski, N.K., et al., *Best practices for generating and using alpha-synuclein pre-formed fibrils to model Parkinson's disease in rodents.* Journal of Parkinson's disease, 2018. **8**(2): p. 303-322.

Supplementary Material

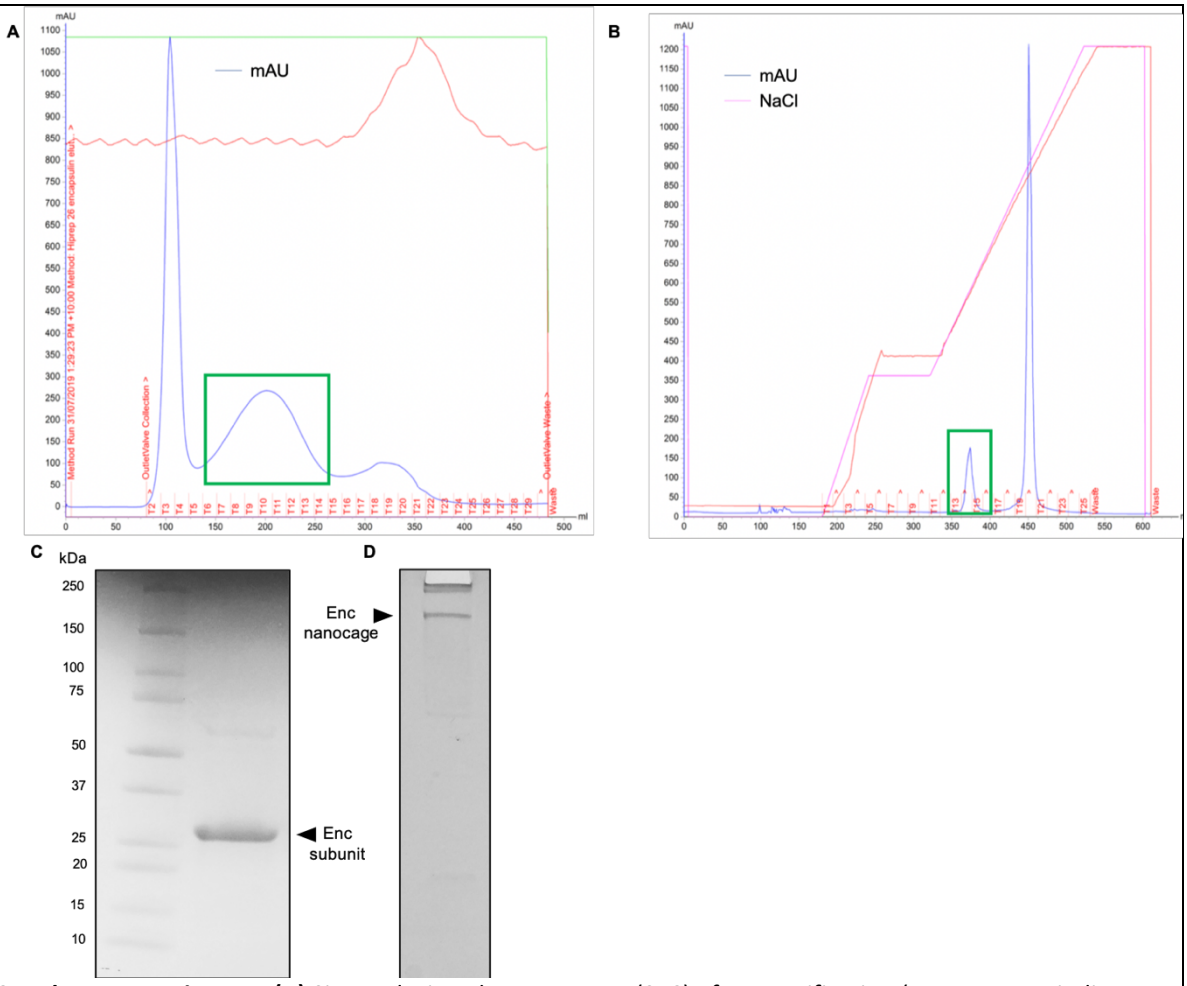

Supplementary Figure 1: (A) Size exclusion chromatogram (SEC) of Enc purification (green square indicates peak corresponding to Enc). **(B)** Anion exchange chromatogram of Enc purification (green square indicates peak corresponding to Enc). **(C)** SDS-PAGE gel showing protein band representing purified Enc subunits at ~31 kDa. **(D)** Native-PAGE gel showing protein band representing purified full nanocage (60 subunits).

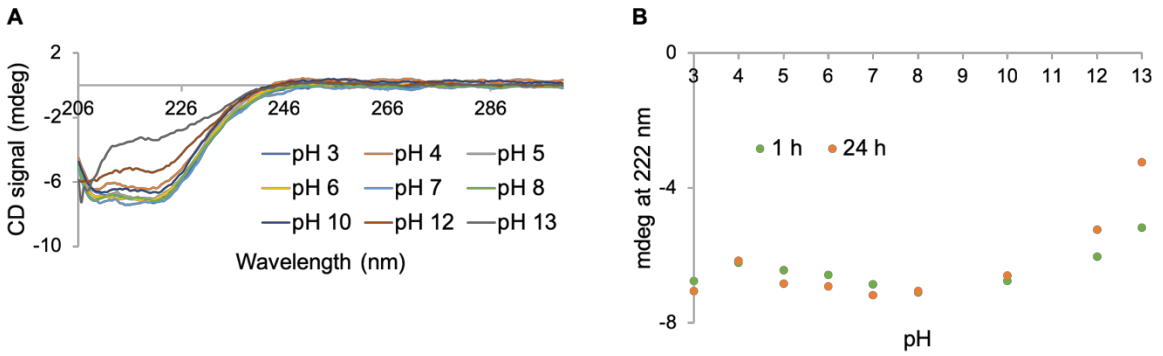

Supplementary Figure 2: CD spectra of encapsulin after being incubated for 24 h in pH 3-13 conditions **(A)** Full CD spectra of Enc after incubation in pH 3-13 showed all pH conditions have minima at approximately 208 and 222 nm, with a significant loss of 222 nm signal at pH 12 and 13 (n = 1). **(C)** CD mdeg at 222 nm comparing encapsulin incubated in pH conditions for 1 h and 24 h showed pH 12 and 13 continued a further loss of 222 nm signal (n = 1).

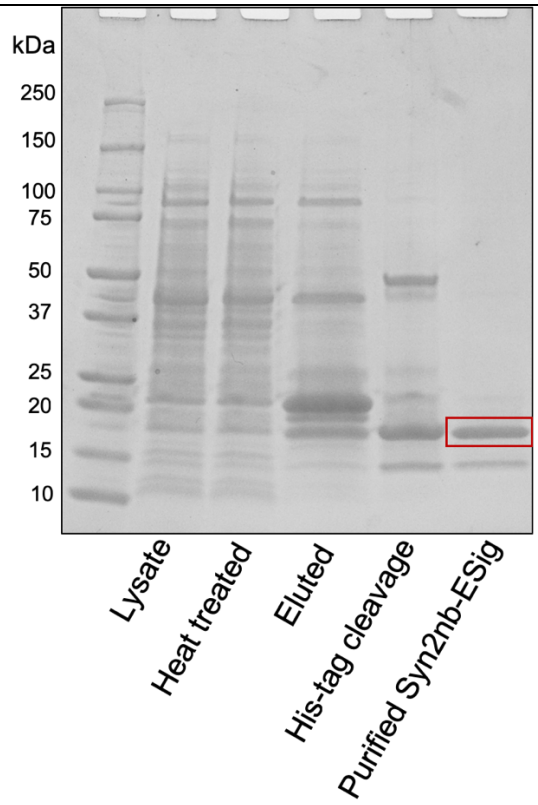

Supplementary Figure 3: SDS-PAGE gel of His-tagged Syn2nb-ESig before and after immobilised metal affinity chromatography (IMAC). A protein band at ~18 kDa showed successful purification and subsequent His-tag cleavage of Syn2nb-ESig.